3-14-2014

Development and Characterization of a High Speed Mid-IR Tunable Diode Laser Absorption Spectrometer for CO and CO_2 Detection in Detonation Events

Stephen D. Wakefield

DEVELOPMENT AND CHARACTERIZATION OF A HIGH SPEED MID-IR TUNABLE DIODE LASER ABSORPTION SPECTROMETER FOR CO AND CO_2 DETECTION IN DETONATION EVENTS

THESIS

Stephen D. Wakefield, Second Lieutenant, USAF

AFIT-ENP-14-M-38

DEPARTMENT OF THE AIR FORCE
AIR UNIVERSITY

AIR FORCE INSTITUTE OF TECHNOLOGY

Wright-Patterson Air Force Base, Ohio

AFIT-ENP-14-M-38

DEVELOPMENT AND CHARACTERIZATION OF A HIGH SPEED MID-IR TUNABLE DIODE LASER ABSORPTION SPECTROMETER FOR CO AND CO_2 DETECTION IN DETONATION EVENTS

THESIS

Presented to the Faculty

Department of Engineering Physics

Graduate School of Engineering and Management

Air Force Institute of Technology

Air University

Air Education and Training Command

in Partial Fulfillment of the Requirements for the

Degree of Master of Science

Stephen D. Wakefield, B.S.

Second Lieutenant, USAF

March 2014

AFIT-ENP-14-M-38

DEVELOPMENT AND CHARACTERIZATION OF A HIGH SPEED MID-IR TUNABLE DIODE LASER ABSORPTION SPECTROMETER FOR CO AND CO_2 DETECTION IN DETONATION EVENTS

Stephen D. Wakefield, B.S.
Second Lieutenant, USAF

Approved:

//signed//	4 Mar 2014
Brian A. Tom, Col, USAF, PhD (Chairman)	Date
//signed//	4 Mar 2014
Glen P. Perram, PhD (Member)	Date
//signed//	3 Mar 2014
Brian C. Sell, PhD (Member)	Date

Abstract

A tunable diode laser absorption spectroscopy system, capable of collecting data at a 10 kHz repetition rate near 4.5 μm, was developed. This system was made feasible in recent years due to the development of quantum cascade lasers active in the 4.5 μm region of the spectrum. Reaching into the mid-IR region of the electromagnetic spectrum allowed for an analysis of the fundamental absorption bands for both CO and CO_2. First, the system was set up such that two lasers, one tuned for CO absorption, the other tuned for CO_2 absorption, propagated collinearly. The intensity for each laser was split in half, with half the intensity passing into an etalon in order to obtain a frequency reference while the other half was passed over a test section. The spectral absorption was measured for ethylene, methane, ethane, and propane across a variety of equivalence ratios, at various heights above a Hencken Burner surface. The features measured were determined to be the P(10) line of the fundamental CO_2 asymmetric stretch absorption and the R(28) of the hot band (v'=4, v"=3) CO absorption. Although measuring a hot band is not ideal, it was adequate due to the high temperatures of the experiment. For each fuel, the concentration of CO_2 was found to agree with chemical equilibrium analysis (CEA) calculations within approximately 8%. The concentration for CO agreed with CEA but with larger error bounds at approximately 20%. It is believed that such large error can be attributed to taking measurements on a hot band, as well as large amounts of H_2O and CO_2 absorption in the area, especially at low equivalence ratios. This ultimately resulted the measurement of combustion efficiency, which agreed with expected results with approximately 10% error bounds. With this system's proof of concept, it will be possible to analyze real combustors as well as detonation events which require a minimum 10 kHz repetition rate.

Acknowledgments

There are many people who made this project and learning process possible for me. I would like to thank Col Tom for originally getting me interested in this project and for not only guiding my academic progress but being a great military mentor as well. I would also like to thank Dr. Brian Sell with whom I worked constantly on this project. His input and help throughout the project was vital. Similarly, the input of Dr. Matt Fotia was vital in my development of the analysis of the data. Finally, I would also like to thank Dr. John Hoke and Dr. Fred Schauer for allowing me to gain valuable experience working with AFRL and in AFRL facilities.

Stephen D. Wakefield

Table of Contents

Page

List of Figures

List of Tables

List of Symbols

Symbol	Definition
I	Intensity ($\frac{\mathrm{W}}{\mathrm{cm}^2}$)
S	Line Strength ($\frac{\mathrm{cm}^{-1}}{\mathrm{molecules\ cm}^{-2}}$)
P	Pressure (atm)
X	Mole Fraction
ϕ_ν	Voigt Line Shape (cm)
L	Length (cm)
α_ν	Absorbance (cm^{-1})
A_i	Integrated Absorbance (cm^{-2})
T	Temperature (K or F)
Q	Partition Function
E	Energy (cm^{-1})
E'	Lower State Energy (cm^{-1})
E''	Upper State Energy (cm^{-1})
ν	Frequency (cm^{-1})
h	Planck's Constant (J s)
c	Speed of Light ($\frac{cm}{s}$)
k	Boltzmann's Constant ($\frac{J}{K}$)
R	Ratio of Integrated Absorbances
k_ν	Spectral Absorption Coefficient (cm^{-1})
ϕ_L	Lorentzian Line Shape (cm)
$\Delta\nu_c$	FWHM for Collisional Broadening (cm^{-1})
b	Pressure Broadening Coefficient
ϕ_G	Gaussian Line Shape (cm)

Symbol	Definition
$\Delta\nu_D$	FWHM for Doppler Broadening (cm^{-1})
M	Atomic Mass (AMU)
V	Potential Energy (cm^{-1})
r	Distance Separating Two Atoms (cm)
D	Dissociation Limit (cm^{-1})
β	Morse Potential Parameter (cm^{-1})
ω_e	Equilibrium Vibration Frequency (cm^{-1})
$\omega_e\chi_e$	Anharmonicity Constant (cm^{-1})
B_e	Effective Rotation Constant (cm^{-1})
D_e	Effective Centrifugal Distortion Constant (cm^{-1})
α_e	Vibration-Rotation Interaction Constant (cm^{-1})
v	Vibrational Quantum Number
J	Rotational Quantum Number
N	Total Concentration
n	Index of Refraction
ϕ	Equivalence Ratio
m	Mass (kg)
ρ	Density (kg/m^3)
$\dot{V}$	Volume Flow Rate (m^3/s)
v_f	Flame Velocity (m/s)
CE	Combustion Efficiency

Subscripts

t	Transmitted
o	Reference

Symbol	Definition
i	Counting Place Holder
v	Frequency Dependence
e	Equilibrium
J	Rotational Quantum Number
st	Stoichiometric Conditions

List of Acronyms

Acronym Definition

TDLAS Tunable Diode Laser Absorption Spectroscopy

IR Infrared

AMU Atomic Mass Unit

LAS Laser Absorption Spectroscopy

LED Light Emitting Diode

QCL Quantum Cascade Laser

DFB Distributed Feedback

TEC Thermo-Electric Cooler

MCT Mercury-Cadmium-Telluride

CE Combustion Efficiency

CEA Chemical Equilibrium Analysis

PDE Pulse Detonation Engine

RDE Rotary Detonation Engine

DEVELOPMENT AND CHARACTERIZATION OF A HIGH SPEED MID-IR TUNABLE DIODE LASER ABSORPTION SPECTROMETER FOR CO AND CO_2 DETECTION IN DETONATION EVENTS

I. Introduction

Absorption spectroscopy as a field has been explored in tremendous detail. Databases (HITRAN, HITEMP, etc) contain vast amounts of information detailing the spectra associated with various atoms and molecules. From these spectra it is possible to determine many useful characteristics of gases such as temperature, pressure, and species concentration. This knowledge provides for a strong theoretical basis for experimental work.

Laser Absorption Spectroscopy (LAS) is one experimental method by which this spectroscopic information is found in the real world. Laser absorption spectroscopy has been used in numerous studies to determine important flow field parameters, such as temperature, pressure, and concentration of gases in combustion reactions. There are many techniques for performing laser absorption spectroscopy, among these techniques is tunable diode laser absorption spectroscopy.

Tunable Diode Laser Absorption Spectroscopy (TDLAS) has been used in various studies and has shown promise for temperature and concentration measurement in combustion devices. These studies have confirmed the experimental technique is valid to find flow field parameters for various devices; however, as with all science, there is still room for improvement in this field.

Most studies up to this point have focused on the near Infrared (IR) region of the spectrum. These choices have been made primarily due to an availability of

telecommunications technology as well as adequate line strength to perform the analysis. However, it has been noted that the mid-IR region contains extremely strong absorption features for CO and CO_2. Due to this, TDLAS in the mid-IR region allows for adequate line strength to accurately determine physical properties in various combustion gases.

Also, because of the complexity of spectra being emitted from combustion devices it is extremely important to focus on absorption lines that will result in the least cluttered data. For absorption spectroscopy on combustion devices, the mid-IR region of the spectrum is significantly less cluttered than the near-IR for CO and CO_2. TDLAS at 4.5 μm will yield stronger absorbances of CO and CO_2 away from H_2O bands that would otherwise result in difficult to interpret data. This region shows absorption profiles for CO and CO_2 that are orders of magnitude stronger than those of H_2O. Because of such strong absorption, these profiles will then be able to more accurately provide information regarding the chemical composition of combustion devices.

To date, one issue with TDLAS measurements of combustion arises from the speed of combustion events. Because the TDLAS system scans across various wavelengths it is an inherently time-limited system. Therefore, up to this point it has been difficult to collect all the information in a combustion event simply because the event time scale is shorter than the scanning time scale.

This research project sought to build a new TDLAS system that is capable of measuring CO and CO_2 absorption lines in the mid-IR region. The system was then used to characterize a known emission spectra from a Hencken burner to find temperature and concentration information. Because the Hencken burner characteristics are so well known, this data was easily compared to known data to verify both the experimental technique and the validity of operating a TDLAS system in the mid-IR region. With proper calibration to the known characteristics of the Hencken burner the system was then run at speeds in

excess of 10 kHZ which was tested to allow for future characterization of detonation events that require such speeds for adequate diagnostics.

II. Theory and Background

2.1 Laser Absorption Spectroscopy

2.1.1 Principles of Laser Absorption Spectroscopy.

Laser spectroscopy is a very simple yet powerful technique. Absorption of photons by molecules is a fundamental concept in physics. As the theory of quantum mechanics and its application to spectroscopy have continued to become more developed, this process of absorption is better understood. The most fundamental equation for absorption spectroscopy follows from the Beer-Lambert Law,

$$(\frac{I_t}{I_0})_\nu = e^{-SPx_i\phi_\nu L}, \tag{2.1}$$

where S is the line-strength of a specific transition (which is ultimately a product of the absorption cross section and partition function), P is the total pressure, x_i is the mole fraction of the absorbing species i, L is the optical path length, and ϕ_ν is the line shape function. In words, this relationship shows that the intensity of a laser passed through a medium will be attenuated due to properties of the medium. These properties ultimately determine how much of the light is absorbed. Mathematically, this is shown by combining S, P, x_i, ϕ_ν, and L into one term called the absorbance, α.

By looking at the integrated absorbance, it is possible to isolate, S, P, x_i, and L from ϕ_ν since $\int \phi_\nu d\nu \equiv 1$ due to normalization. Therefore, we can express the integrated absorbance as [20]

$$A_i = \int \alpha_\nu d\nu = Px_iS_i(T)L. \tag{2.2}$$

The line strength S, at line center, is given by the equation,

$$S(T) = S(T_0)\frac{Q(T_0)}{Q(T)}(\frac{T_0}{T})e^{[-\frac{hcE''}{k}(\frac{1}{T}-\frac{1}{T_0})]}[1-e^{(\frac{-hc\nu_0}{kT})}][1-e^{(\frac{-hc\nu_0}{kT_0})}]^{-1}, \tag{2.3}$$

where $Q(T)$ is the partition function, $E''[cm^{-1}]$ is the lower-state energy, $\nu_0[cm^{-1}]$ is the line-center frequency, T_0 is the reference temperature, and $h,\ c,\ k$ are Planck's constant, speed of light, and Boltzmann's constant, respectively [24].

With this relation it is then possible to determine the temperature based on a two line technique [11]. By taking the ratio of the integrated absorbances of two molecular transitions the resulting equation for temperature is,

$$T = \frac{\frac{hc}{k}(E_2'' - E_1'')}{\ln R + \ln \frac{S_2(T_0)}{S_1(T_0)} + \frac{hc}{k}\frac{(E_2''-E_1'')}{T_0}}, \tag{2.4}$$

where R is the ratio of integrated absorbances, E_1'' and E_2'' are the respective lower-state energies, and $S_1(T_0)$ and $S_2(T_0)$ are the line strengths at reference temperature T_0.

With a known temperature, it is then possible to determine the concentration of other absorbing species. The spectral absorption coefficient can be defined as [11]

$$k_\nu = P x_{abs} S_i(T) \phi_\nu, \tag{2.5}$$

and can be found solving equation 2.1

$$k_\nu = P x_{abs} S_i(T) \phi_\nu = -\frac{\ln \frac{I_t}{I_0}}{L}. \tag{2.6}$$

With a known temperature the line strength can then be corrected to the line strength at that temperature using equation 2.3 and with a known pressure the only parameters that remain unknown are the mole fraction of the absorbing species x_i and the line shape ϕ_ν.

The line shape for the spectroscopic transitions of interest are approximated by a Voigt profile. The Voigt profile is a convolution of a Gaussian profile with a Lorentzian profile. As such it takes into consideration spectroscopic broadening due to both collisional effects and Doppler effects. The collisional effects follow a Lorentzian distribution given by

$$\phi_L = \frac{\Delta\nu_c/2\pi}{(\Delta\nu_c/2)^2 + (\nu - \nu_0)^2}, \tag{2.7}$$

where ν is the frequency, ν_0 is the center frequency of the distribution, and $\Delta\nu_c$ is the full width at half max (FWHM) given according to

$$\Delta\nu_c = bP, \tag{2.8}$$

where b is the pressure-broadening coefficient. The Doppler effects are governed by a Gaussian profile given by

$$\phi_G = \frac{2}{\Delta\nu_D}\sqrt{\frac{\ln 2}{\pi}}e^{-4\ln 2((\nu-\nu_0)/\Delta\nu_D)^2}, \tag{2.9}$$

where ν and ν_0 are defined as they are above, and

$$\Delta\nu_D = 7.2\times10^{-7}\tilde{\nu_0}\sqrt{\frac{T}{M}}, \tag{2.10}$$

where T is temperature in K, M is atomic mass in Atomic Mass Unit (AMU), and $\tilde{\nu_0}$ is the frequency in cm^{-1}. The Voigt profile can then be determined according to,

$$\phi_\nu = \int_{-\infty}^{\infty}\phi_L\phi_G d\nu. \tag{2.11}$$

Furthermore, with the measurements made perpendicular to the gas flow on fundamental bands, there were no frequency shifts in the absorption profile. With these factors in place the mole fraction of the absorbing species can then be found through simple algebraic manipulation of Equation 2.6 [4].

2.1.2 Benefits of LAS.

Although laser absorption spectroscopy typically requires sophisticated instrumentation, it holds several advantages over standard spectroscopic experiments. First of all, the absorption coefficient α is frequency dependent [8]. This eliminates the need for a monochromator; replacing it instead with a tunable laser source. With an adequately narrow bandwidth laser (i.e. a single mode laser) the resolution of the experiment is then dependent on the interrogated transition itself rather than instrumentation [8]. Furthermore, lasers have a high spectral power density [8]. In essence, this allows the signal-to-noise ratio of the experiment to be limited by the laser and not the detectivity of the detector. Also,

the actual profile of the absorption can be measured [8]. With the superior resolution of LAS the detectivity of the experiment is increased, allowing for measurement of the entire transition profile. This measurement allows for sufficient information to adequately determine broadening coefficients. Finally, with LAS it is possible to measure high speed transient events. Not only can pulsed lasers be tuned over transitions very rapidly [8], but continuous wave diode lasers are capable of tuning over transitions at several kHz. Traditionally, high speed lasers can be used to measure "short-lived intermediate radicals in chemical reactions," [8], but this study sought to show that lasers operating at high speeds will allow for accurate measurements of combustion events.

2.2 Tunable Diode Lasers

2.2.1 Diodes.

Diodes are simple p-n junction semiconductors. These junctions are created from placing a p-type, or acceptor material, with a n-type, or donor material. When a current is applied to the semiconductor, electrons flow from the donor to the acceptor. The state in which the electrons and holes combine is a lower energy state than the state in which they are separate. The transition from the higher energy level to the lower energy level results in spontaneous emission of light. This process results in a Light Emitting Diode (LED). At relatively low currents, this spontaneous emission also stimulates emission, however, the stimulated emission is "canceled" by stimulated absorption. However, as the current applied across the semiconductor is increased, the junction reaches a point where the stimulated emission dominates the stimulated absorption. At this point, known as threshold, increasing the current results only in increased stimulated emission. When the diode operates above threshold conditions it operates as a laser and any increase in current will effectively result in a proportional increase in laser output power.

Relatively recent advances in technology have enabled diode laser technology to lase in the mid and far-infrared regions of the spectrum. This has been achieved with

a QCL. QCLs operate under the same basic principles as conventional laser diodes with a few distinct differences. Instead of a simple p-n junction, QCLs are built out of multiple quantum semiconductor structures [5]. Each quantum structure varies slightly in composition. This ultimately results in a stair step potential across the entire bulk material as shown in Figure 2.1. Instead of a single recombination process from conduction

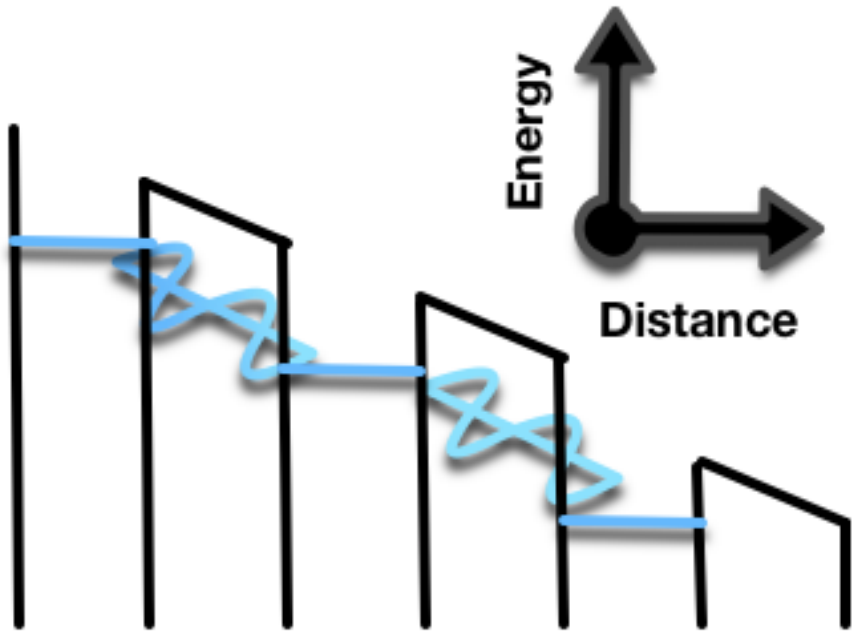

Figure 2.1: The stair step potential of a QCL. Multiple quantum structures allow for a single electron to transition down an energy level then tunnel to the next structure, ultimately resulting in multiple photons produced for a single electron. Figure adapted from Faist [10].

to valance band, such as occurs in a conventional laser diode, the multiple quantum semiconductor structures allow for a single electron to recombine with a hole on one stair step, emitting a photon, and then tunnel through the potential barrier to the next stair step and repeat the process [10]. This process results in a single electron emitting multiple photons in a cascade effect, which ultimately allows for QCLs to emit much more power than conventional diodes.

2.2.2 Tuning a Diode Laser.

The ultimate goal of LAS is to see absorption features at a particular wavelength compared with another wavelength where absorption does not occur. This necessitates a need to tune the wavelength of the laser that is interrogating the medium of interest. Since conventional laser diodes and QCLs both operate under the same basic principles, this discussion will refer to conventional laser diodes for simplicity's sake; however, the same reasoning can be applied to the band gaps/energy differences for QCLs.

Diode lasers are tunable because of how their physical properties change due to thermal changes. There are two ways to tune a diode laser, by temperature control or by current control. Both of these methods ultimately result in thermal changes to the semiconductor. Temperature changes cause changes to the band gap structure of the semi conductor. The change in the band gap structure changes the index of refraction of the semiconductor. This thermal change causes the Bragg reflector on the diode to alter which wavelength is chosen for lasing [14]. Changing the temperature on the diode itself is a relatively slow process and the same thermal changes can be accomplished much more quickly through current tuning. Changing the current through the semiconductor results in Joule-heating effects as the current is increased. This changes the temperature of the diode and once again causes a change in the refractive index.

Mode hopping is undesirable in most laser applications. In lasers in which the longitudinal mode spacing is adequately narrow, it is possible when tuning to jump from one longitudinal mode to another. This results in an abrupt jump in wavelength tuning instead of the smooth tuning necessary for an LAS experiment. This jump to a different longitudinal mode occurs because the refractive index and the band gap of the semiconductor do not have the same dependence on temperature [14]. This results in the overall gain profile of the laser tuning at a different rate than the longitudinal modes. Thus as the peak of the gain profile overtakes a different longitudinal mode, the wavelength will

jump to the new mode. A simple graphic of this phenomenon is shown in Figure 2.2. This phenomenon can and should be avoided by characterization of any diode to be used in LAS, along with appropriate absorption line selection for a specific laser.

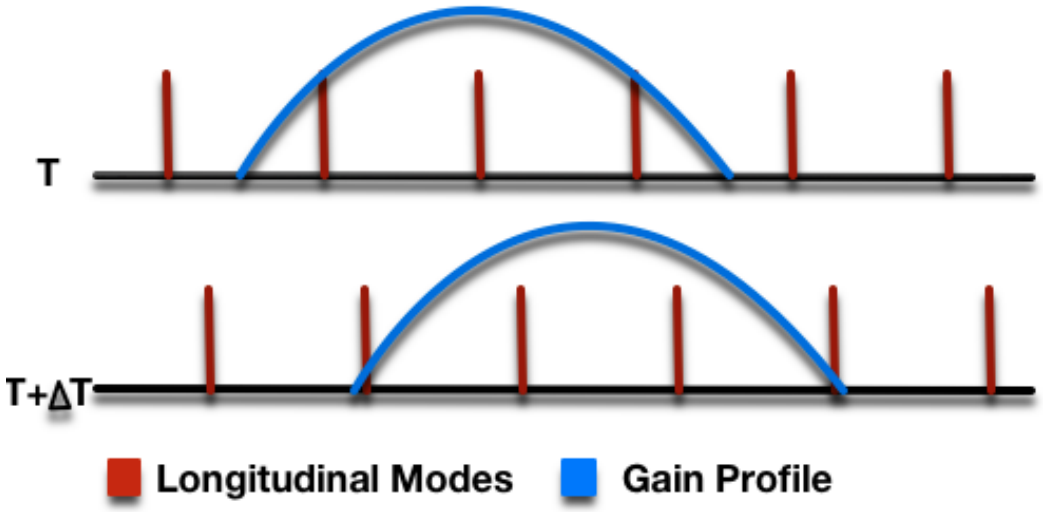

Figure 2.2: A simple graphic that illustrates that as the gain profile and longitudinal modes shift at different rates, eventually a different longitudinal mode will dominate the lasing process. Figure adapted from Heumier [14].

2.3 Line Selection for CO and CO_2

The first step in any absorption experiment is to determine which absorption lines of each species are going to be investigated. There are two main factors that go into this determination. First, the absorption feature itself should be a strong enough absorption that it can be detected. Secondly, the more isolated the absorption line is from other absorption lines from the same or different species, the easier it will be to gather useful information from the data. The second factor is a matter of simply finding features that are isolated; however, in light of the first factor, it is possible to determine where the strongest absorption features will occur with relative ease.

Determining the strength and position of molecular absorption features comes from solving Schroedinger's equation for each specific molecule. For the CO molecule this is done by approximating the molecule as a vibrating rotor. Calculation yields a potential defined by the Morse potential,

$$V(r) = D(1 - e^{-\beta(r-r_e)})^2, \tag{2.12}$$

where D is the dissociation limit, β is the Morse potential parameter, r is the time-dependent distance between the two atoms, and r_e is the equilibrium distance between the atoms [4]. For this potential, the energy eigenvalues are defined as,

$$E(cm^{-1}) = \omega_e(v+\frac{1}{2}) - \omega_e\chi_e(v+\frac{1}{2})^2 + B_eJ(J+1) - D_e(J(J+1))^2 - \alpha_e(v+\frac{1}{2})J(J+1), \tag{2.13}$$

where ω_e is the equilibrium vibration frequency, $\omega_e\chi_e$ is the anharmonicity constant, B_e is the effective rotation constant, D_e is the effective centrifugal distortion constant, α_e is the vibration-rotation interaction constant, v is the vibrational quantum number, and J is the rotational quantum number. Although there are higher order terms that play into this equation, this simplification serves simply to demonstrate the general location of the fundamental absorption band.

Determination of the absorption intensity starts with a simplified case from which it is possible to logically extend that case to the more complicated real world scenario. If the rotational transition of a molecule is examined, the line intensity is determined by the dipole moment and the population difference between the two rotational energy levels [4]. In this case, the population of each rotational transition can be statistically calculated as,

$$N_J = N(2J+1)\frac{(B_e - 1.5\alpha_e)e^{-(B_e-1.5\alpha_e)J(J+1)/kT}}{kT}, \tag{2.14}$$

where N is the total concentration, B_e and α_e are defined as in the Equation 2.13, k is the Boltzmann constant, T is temperature, and J is the rotational quantum number [4]. This intensity distribution yields a Boltzmann like distribution. Once again, this Boltzmann

distribution is a simplification for the purposes of this argument. A rigorous simulation would need to account for higher order terms to include the centrifugal distortion, D_e; however, to find the general location and obtain relative intensities these terms can be left out. For example given the values for CO [12] of $B_e = 1.9303\ cm^{-1}$, $\alpha_e = 0.0175\ cm^{-1}$, $\omega_e = 2168.25\ cm^{-1}$, and $\omega_e\chi_e = 13.27\ cm^{-1}$, yields a distribution and absorption stick spectrum as shown in Figure 2.3.

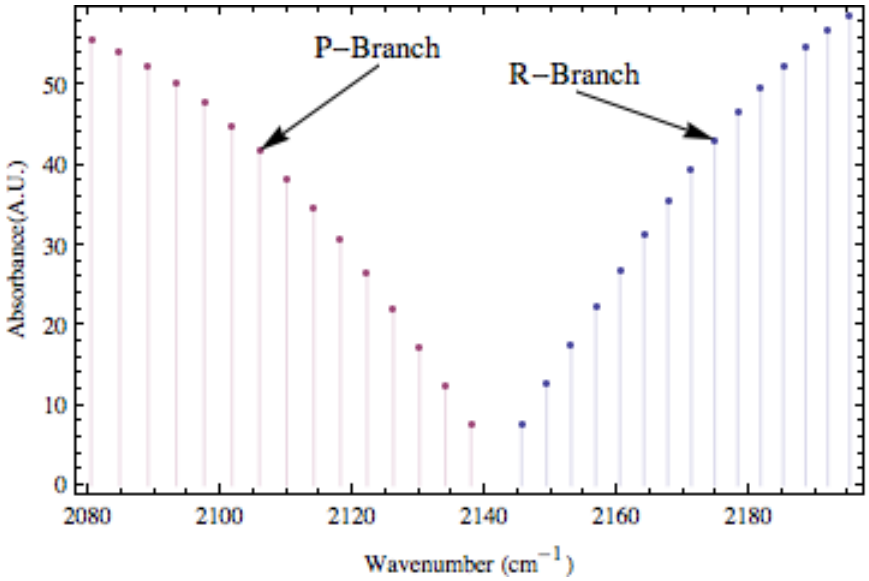

Figure 2.3: A simulation of the fundamental spectrum for CO. This spectrum shows the positioning of the CO absorption in the region of interest and also provides an basis for how the absorption intensity is distributed in the P and R branches.

When the vibrational energy levels of the molecule are taken into account more than just the dipole moment and population differences affect the absorption distribution. However, this experiment was simply concerned with choosing which lines would yield the greatest absorption. With this in mind, it is possible to choose the vibrational absorption band based on qualitative assumptions rather than quantitative. Selection rules for rovibrational transitions allow for a $\Delta v = \pm 1, \pm 2, \pm 3, etc$; however, the strongest absorption will occur in the fundamental transition, that is the transition with $\Delta v = \pm 1$

from the ground state. [4]. The fundamental rovibrational transition for CO is shown by Equation 2.13 and the simulation in Figure 2.3 still represents an adequate simulation for this choice. Therefore, an absorption line around 4.6 μm is an ideal choice.

Theoretically determining the absorption line to probe for CO_2 is a more complicated process. Because CO_2 is a polyatomic molecule, its spectrum becomes much more complicated than the spectrum for a diatomic molecule. Once again, the absorption to be examined should be in the fundamental band in order to yield the greatest absorption in the experiment; however, the added complexity of three atoms making up the molecule lead to more degrees of freedom that ultimately result in multiple fundamental bands. Not only can a molecule now rotate and vibrate, but the vibrations can occur symmetrically (as in symmetric stretch) or asymmetrically (asymmetric stretch) and the molecule can bend symmetrically or asymmetrically as shown in Figure 2.4. It is therefore necessary to

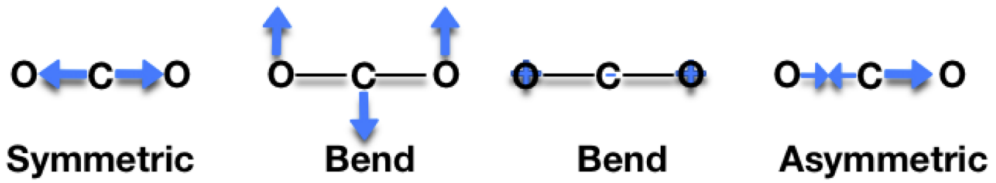

Figure 2.4: A graphical illustration of the different modes in a CO_2 molecule. The "third" atom added to the molecule greatly increases the spectral complexity. Figure adapted from Engel [9].

choose a transition that is active in the infrared region of interest. For CO_2 the asymmetric stretch mode is active near 4.5μm. Because this is a stretching mode in a linear molecule, it behaves similarly to the infrared spectrum of diatomic molecules, such as CO [4]. Along with its relatively strong absorption, the placement of this band makes it an adequate choice for mid-IR TDLAS shown in Figure 2.5. For the simulation in Figure 2.5, HITEMP was used due to the inaccuracy of the HITRAN database at high temperatures; however, even the HITEMP database has inaccuracies in the mid-IR region. This investigation relies

on the accuracy of HITEMP for the fundamental bands, but may be used to verify other absorption lines in the area.

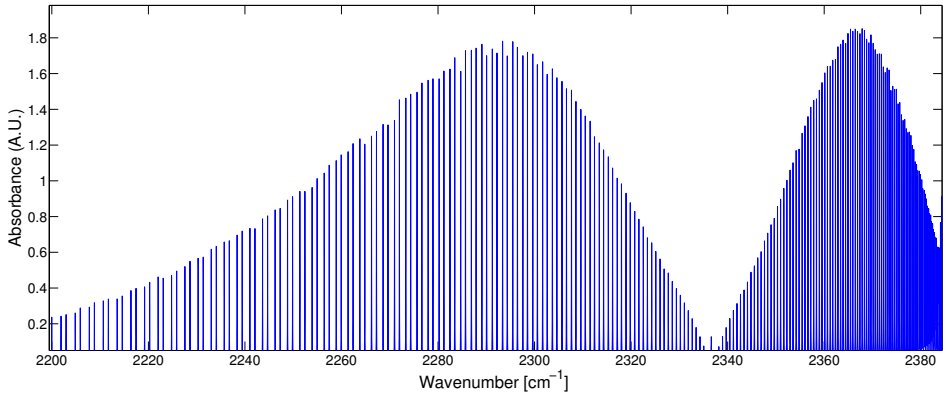

Figure 2.5: A HITEMP Simulated stick spectrum (position and relative intensity only) of the asymmetric stretch transition near 2300 K. This is a fundamental transition in the region of interest and thus yields enough absorption to accomplish the experiment [25].

2.4 Previous Research

2.4.1 Hencken Burner.

There has been a substantial amount of research characterizing the Hencken burner flame which made it a very good choice for characterizing the mid-IR system. This research focused on other methods of spectral analysis yielding results for temperature at various locations in the flame. This research served a baseline to which the experimental results of this work could be compared [19, 21]. There have also been many investigations that have examined concentrations of combustion constituents on the Hencken burner. However, these investigations have focused on other methods of spectral analysis [15, 18].

2.4.2 TDLAS.

The Hanson group at Stanford has done extensive research using TDLAS to characterize combustion. Using rovibrational spectra in the near-IR region, they

were able to obtain results in agreement with the HITRAN database for the absorption coefficient for CO as a function of temperature [20]. They also demonstrated the ability to fiber couple lasers for the TDLAS system which will be crucial in the acoustic environment surrounding detonation engines [23]. Further developments in the field have yielded measurements for H_2O and CO_2 concentrations, to include H_2O measurements at 30 kHz as well as measurements in internal combustion engines, turbines, and scramjet engines [6, 7, 13, 16, 17, 22, 26, 30]. In fact, the technique, at least in the near IR region, has become so mature as to be commercialized by several different organizations for measurement applications [6]. Many of these investigations have focused on temperature [13, 22, 30]. There have been systems that have focused on concentrations. However, the systems in the mid-IR region have not performed analysis on a Hencken burner. Also, none of these systems have acquired mid-IR data at 10 kHz. Instead these systems were calibrated with a heated pressure cell [20]. This technique makes it possible to artificially create conditions that are easy to calibrate against. Eventually, this technique should be employed for the system in this investigation.

III. Experimental Setup

3.1 Mid-IR TDLAS

3.1.1 Laser Set-Up.

Recent developments in laser technology have made it possible to conduct TDLAS in the mid-IR region at high repetition rates. In this experiment, the two lasers that were used were Distributed Feedback (DFB) QCLs. The first laser was a Thor Labs QD4580CM1 which operated at approximately 4.58 μm. The second laser was a Thor Labs QD4410CM1AS which operated at approximately 4.41 μm. DFB lasers tend to have extremely narrow laser line widths, less than 3 MHz, which makes them ideally suited for TDLAS [29]. Both of these lasers were two-tab c-mount designs. It was therefore necessary to modify an existing laser diode head in order to adapt from the single tab c-mount style diode to the two tab c-mount due to a lack of availability of two-tab, thermo-electrically cooled diode heads with enough power and temperature control to operate these lasers. The diode heads were Arroyo Instruments 242 high power, thermo-electrically cooled heads. The modification to these heads can be seen in Figure 3.1, which essentially electrically connected the anode of the c-mount to the Laser Diode Driver anode, which had previously been electrically connected to the body of the c-mount. The diode heads were operated by an Arroyo Instruments 4200 Laser Source laser diode driver and an Arroyo Instruments 5305 Thermo-Electric Cooler (TEC) Source thermo-electric cooler. These sources were rack mounted in order to be portable in the future, as seen in Figure 3.2. Also as a part of the rack mount, was a NI PXIe-1085 express chassis. This served as the mounting for the data acquisition hardware, user interface, as well as the function generator in order to drive the lasers.

Next, because both lasers are c-mount design, the lasers had to be collimated. When left uncollimated the both lasers had an approximate 50° longitudinal divergence and a 30°

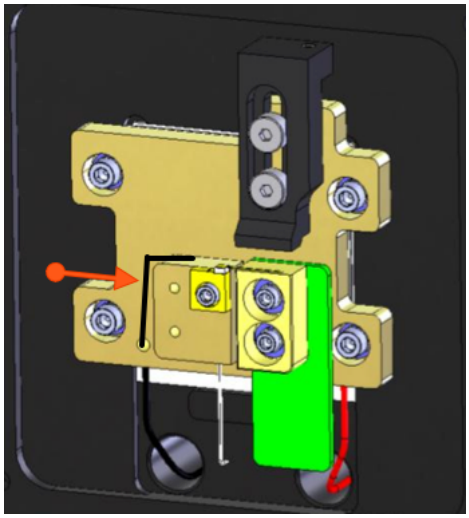

Figure 3.1: Simple modification made to the Arroyo Instruments 242 diode head. Since the metal plate itself acts as the anode for the laser diode a wire is simply run from the anode tab of the two tab c-mount to a small screw placed in the metal plate attached to the TEC.

Figure 3.2: The rack mounted laser drivers and Thermo-Electric Coolers (TECs) that control the lasers in the experiment. The experiment was originally planned for four lasers; however, only two lasers were used. The top two laser drivers were the drivers in use, and the bottom two TECs were the TECs in use.

lateral divergence. In order to take the light emitted from the DFB QCL cavity and place it into a well collimated beam, a Thor Labs C037TME-E aspheric lens was used. These lenses were anti-reflectively coated for wavelengths from 3 μm to 5 μm which ensured minimal back reflection into the cavity itself. With an effective focal length of 1.873 *mm* it was necessary to have precise alignment to ensure well collimated light while also taking care not to touch the laser cavity itself. In order to accomplish this precise placement, the aspheric lenses were placed on cage-mounted x, y, and z stages as seen in Figure 3.3.

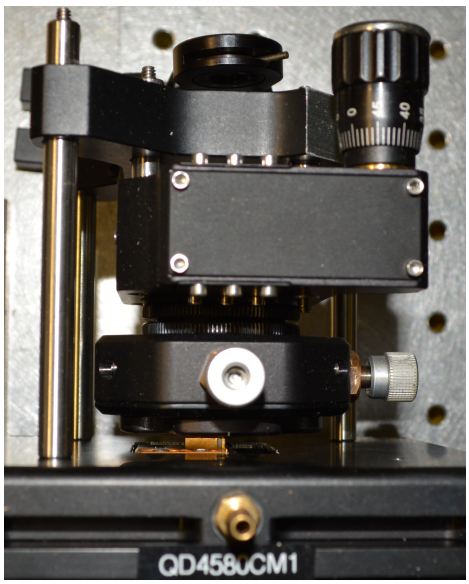

Figure 3.3: This cage mounted stage allowed for precise placement of the asphere lens. The x, y stages controled beam steering, which allowed for straight and level propagation. The z stage allowed precise placement of the asphere a focal length away from the laser diode, which resulted in a well collimated beam.

These stages allowed for accurate positioning of the aspheric lens at one focal length away from the cavity while also giving beam steering capability. The end result was a beam that had negligible divergence over the beam path and approximately a 4 *mm* spot size.

3.1.2 Laser Propagation.

The two separate lasers were combined into the same path through the use of an Edmund Optics ZnSe wire grid polarizer. By physically rotating one of the laser diodes 90° with respect to the other it was possible to use a wire grid polarizer to combine the beams. The first laser, set to probe CO absorption near 4.58 μm was set so that its polarization was vertical and in line with the wires in the polarizer. This allowed for nearly all of the light to be transmitted through the optic. The second laser, set to probe CO_2 lines near 4.41 μm, was set with polarization horizontal so that nearly all of its light was reflected off of the polarizer. Also, in order to ensure two more degrees of freedom on the beam steering, a silver mirror was added into the second laser's propagation path.

After combination through the polarizer, it was necessary to ensure the two lasers were collinear in space. This ensured that the two lasers probed the same line of sight in the test section as well as ensuring that both lasers properly hit the detector. Once the beam from the CO laser was propagating level and straight it was considered the control laser and it was necessary to align the CO_2 laser to be collinear. This was accomplished through small adjustments to both the x-y placement of the aspheric lens as well as the mirror placed in the optical train before the wire grid polarizer. By adjusting all 4 degrees of freedom simultaneously, it was possible to achieve a straight and level laser that propagated collinear to the first laser. Using commercialized thermal paper it was possible to see the beam spot created by the laser. As each degree of freedom was adjusted it was monitored in both the near field (just after the diode) and the far field (approximately 1 meter away). When the beam spot of the laser stayed constant and level it was determined to be well collimated and level.

After the two beams were made collinear, they were passed through a CaF_2 beam splitter. Figure 3.4 shows the reflectance and transmittance of this beam splitter as a function of wavelength. It was clear that for the wavelengths at which these lasers operated

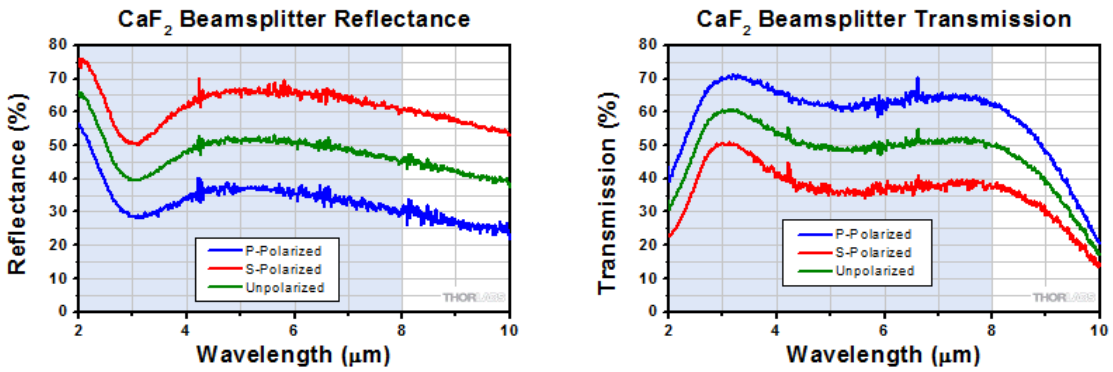

Figure 3.4: Reflectance (a) and Transmission (b) of CaF_2 as a function of wavelength at an angle of incidence of 45° as given by the manufacturer. These graphs show that for the lasers in this experiment nearly 35% will be transmitted and 65% reflected [1].

that CaF_2 was the most readily available, commercial off the shelf choice. From the beam splitter, half of the beam was pitched through an etalon and into a detector, while the other half was pitched through the test section into the detector.

3.1.3 Etalon.

The etalon used was a 170 *mm* CaF_2 etalon with polished ends. The etalon was 170 *mm* due to manufacturing limitations; however, this length still provided enough free spectral range in order to accurately determine wavelength. The free spectral range of an etalon is given by

$$\Delta\nu = \frac{c}{2nL}, \tag{3.1}$$

where $\Delta\nu$ is the peak spacing in Hz, c is the speed of light, n is the index of refraction for the etalon, and L is the length of the etalon. With a refractive index of approximately 1.4, a CaF_2 crystal of this length yields a free spectral range of $\Delta\nu = 630MHz$ which in wavelength is $\Delta\lambda = 0.0425\ nm$. This free spectral range came into play when determining the wavelengths that the lasers were probing. Although other etalons are available for the wavelenghts used in this investigation, it was necessary to have a solid etalon with coatings due to original experiment designs. Originally, H_2O absorption was going to be measured

simultaneously near 1.4μm. This CaF_2 etalon was adequate to for both the 1.4μm and 4.5μm regions of the spectrum.

3.1.4 Detectors and Signal Acquisition.

Both detectors were Infrared Associates MCT-5-0.5PV. These detectors were Mercury-Cadmium-Telluride (MCT) photo-voltaic conductors. MCT detectors are sensitive from 2 μm to 5 μm as shown in Figure 3.5, which ensured that lasers operating near 4.5 μm fell well within the linear detection range. Liquid nitrogen cooling ensured the MCT element was adequately cooled and ultimately lead to a better signal to noise ratio for the detectors. A Thor Labs 2A5315-E anti-reflection coated plano convex lens was placed in

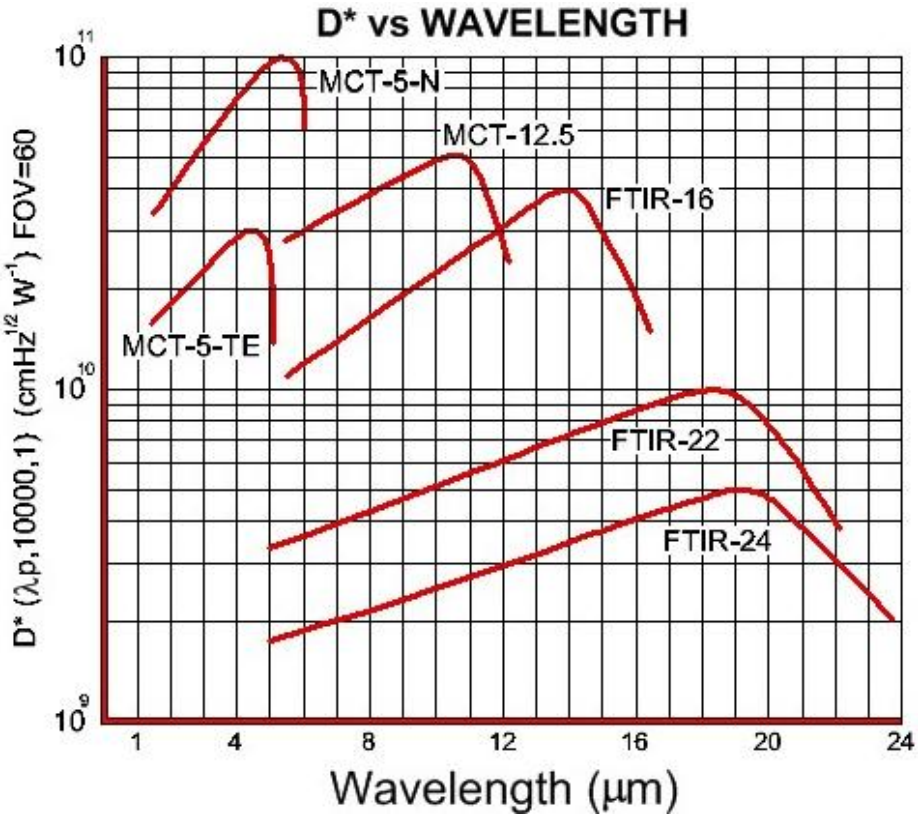

Figure 3.5: Detectivity range for Mercury-Cadmium-Telluride (MCT) along with other semiconductor detectors. Liquid cooled MCT detectors provide better detectability than TEC cooled detectors [2].

front of each detector. This allowed for focusing onto the 0.5×0.5 *mm* MCT element to ultimately avoid any non-linear effects near the edges of the element. However, for this experimental setup the aspheric lens was used to overfill the detector, by creating a larger beam size, to avoid saturation by having a less intense beam hitting the final element. Overfilling the detector also helped to mitigate any effects that occurred due to beam steering within the flame. Furthermore, wire mesh was used as a neutral density filter in order to cut down the laser intensity to avoid saturation. Also, a set of irises was placed in front of each detector to spatially filter the input. This was necessary due to the sensitivity of the detectors as they would pick up background IR radiation in the lab. The full experimental set up is shown in Figure 3.6. The detectors were then connected to channel 'A' of Stanford Re-

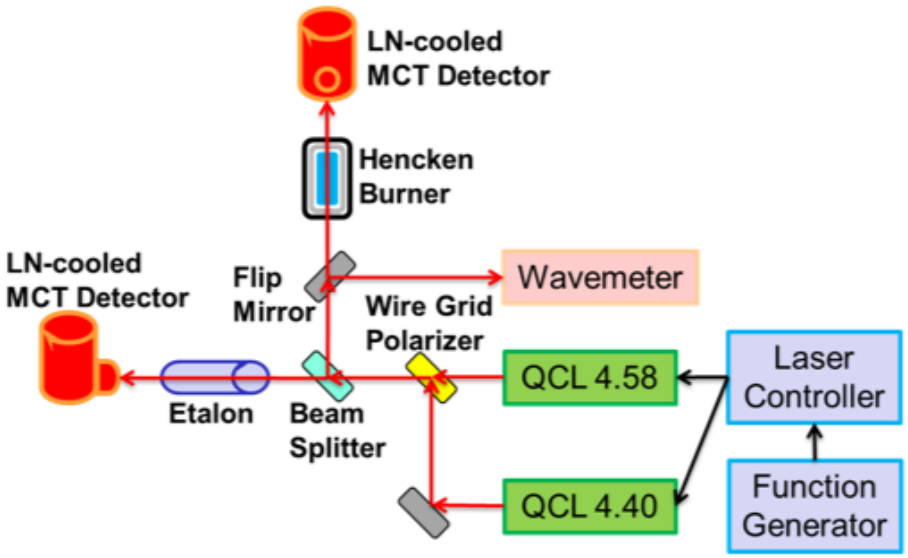

Figure 3.6: Each laser was controlled by Arroyo Instruments laser controllers. Using a wire grid polarizer the two lasers were combined using a wire grid polarizer. From the polarizer the beams passed through a CaF_2 beamsplitter. Half the signal passed through an etalon to determine the frequency content of the laser, while the other half is passed over the test section for absorption measurement. The incident intensity was determined by passing the lasers over the test section without the Hencken burner running. Also, to determine the tuning characteristics of the lasers, a flip mirror was used to intercept the test section beams and pass them to a wavemeter.

search Systems SR560 current pre-amplifiers. Also, connected to each pre-amplifier was a custom built, variable voltage output box. This box was constructed using a simple variable voltage divider with a power supply, potentiometer, and resistor, as seen in Figure 3.7. Because each detector had a slight offset, it was necessary to connect this variable voltage

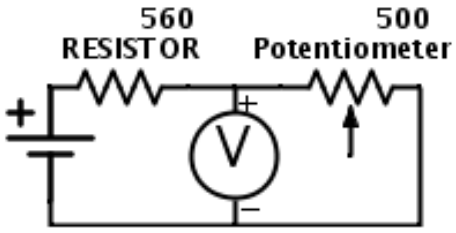

Figure 3.7: Wiring schematic of the custom-built variable voltage output box. A simple voltage divider with one resistor being a potentiometer allowed for variable voltage output. The box was attached to the second channel of an SRS pre-amp in order to adjust the offset voltage of the detector.

box to channel B of the preamplifier and then use the pre-amplifier to subtract the offset from each detector. This allowed the baseline signal coming from the detectors to be tuned to zero volts.

Having the voltage centered around zero volts was necessary for the data acquisition hardware. For data acquisition, a high speed NI5734 was used. The card was a 16 bit card in a PXI chassis with a high speed bus that accepted input voltages between -1 and +1 volts. Therefore, in order to obtain as much resolution as possible, it was necessary to center the signal in this range using the custom built voltage box along with the pre-amplifiers.

3.1.5 Wavemeter.

In order to make use of the etalon, to be discussed in the analysis section, it was necessary to find the wavelength ranges in which the laser diodes were operating. In order to do this, a silvered mirror was placed on a 90° flip-mount. This flip-mount was then placed to where, when engaged, the mirror would effectively intercept the laser beam and pitch it to another mirror. This second mirror was then used to steer the laser inside a Bristol 621A

wavemeter. The Bristol is sensitive from 1 μm to 5 μm with a maximum power of 10 mW. The Bristol emitted a low power, red alignment laser. In order for the interferometer inside the Bristol to work properly and the instrumentation accurately determine wavelength, the diode laser beams and the red alignment laser must be collinear. Therefore, it was necessary to first align the diode laser so that it entered the wavemeter. After this alignment was complete, the Bristol was adjusted, while keeping the input aperture fixed, so that the alignment laser was collinear.

With the Bristol wavemeter properly aligned, it was then necessary to determine how the wavelength of each laser diode tuned as a function of both temperature and driving current. To find these relationships, the laser thermo electric controller was set to a particular temperature. With the temperature set the laser was then tuned by adjusting the current from just above threshold to slightly below the maximum current through the laser driver while the wavelength of the laser was recorded with the Bristol software. This process was then repeated for several different temperatures for each laser. The results are summarized in Figure 3.8.

These results were useful; however, they were not implemented themselves. The wavelengths returned from this process were used simply to determine the general area of the electromagnetic spectrum where the laser operated. Due to adverse heating effects from rapidly turning on and off the laser while running at a 10 kHz repetition rate the temperatures and currents detailed in Figures 3.8 did not directly correspond to what was observed. Also, due to the high repetition rates, lower temperatures and currents had to be used in order to ensure that each laser was turning all the way off while the other laser was on. If both lasers were on at the same time not only was each spectrum convoluted but additional interference occurred in the etalon. Thus, additional data were taken to determine the wavelength of the absorption features being observed. Each laser was turned on at a 10 kHz repetition rate at a given temperature and current and a spectral feature was

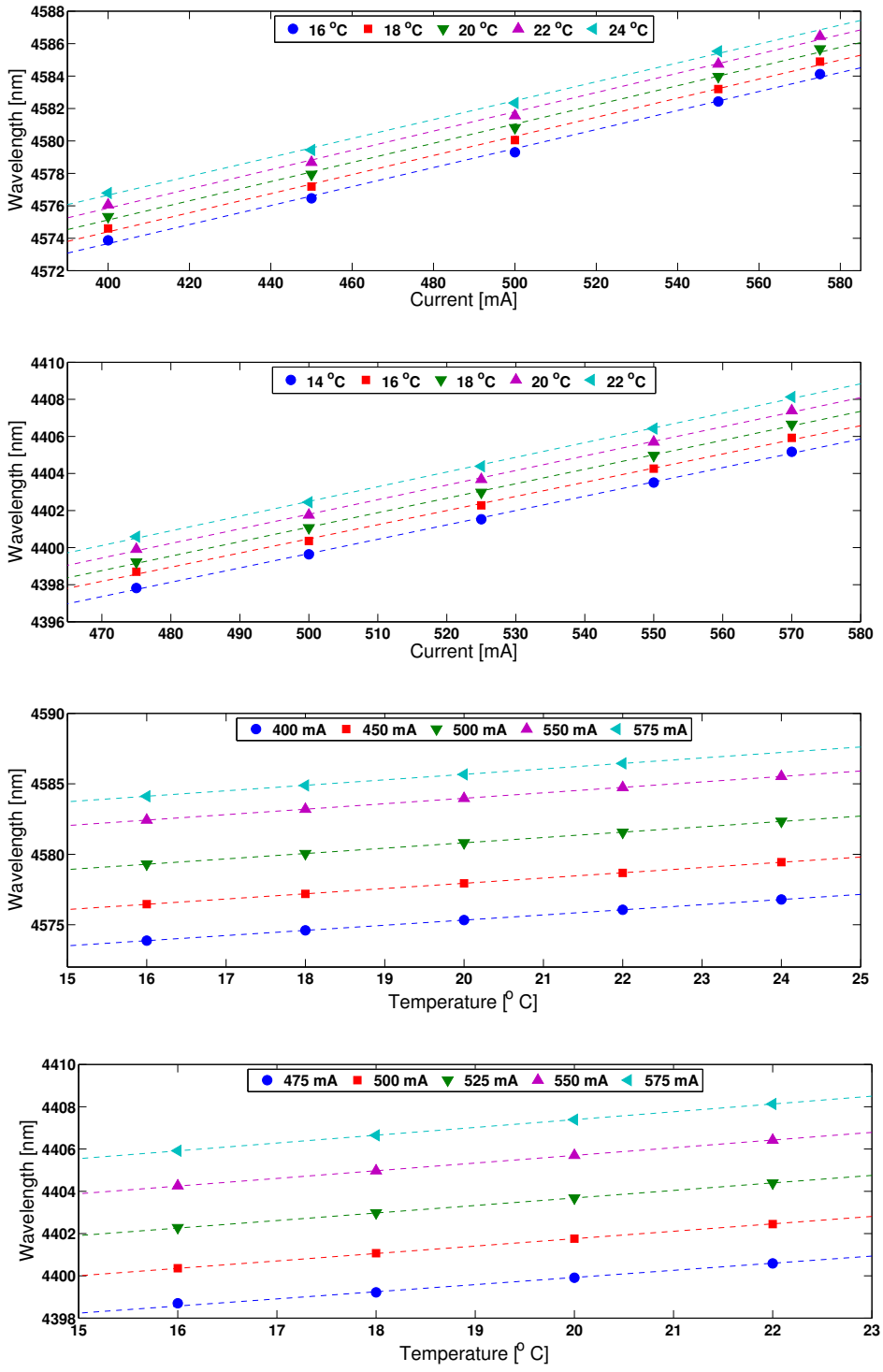

Figure 3.8: These plots indicate the tunability of the two lasers in the experiment. (a) shows how the 4.58 μm laser tuned with changing current, while (b) indicates tuning with current for the 4.41 μm. (c) and (d) show tuning with temperature for each laser respectively. All plots are linear with the smallest R^2 value being 0.9971 which was to be expected [28].

identified. Then in order to determine the wavelength of that spectral feature the repetition rate was cut in half. With half the repetition rate, the laser behaved differently due to heating effects. To counter the change in behavior the temperature and current were changed so that the same spectral feature as identified at 10 kHz was observed. This process continued, cutting the repetition rate in half until the lasers were operating at approximately 0.3 Hz. A repetition rate this slow allowed for the wavemeter to be used to identify the wavelength sweep.

With the features identified it was then necessary to test the maximum data acquisition repetition rate of the system. As the lasers were run at higher repetition rates, the time it takes for the laser to turn off became more of an issue. The QCL could not drop below threshold instantaneously. When both QCLs were on at the same time, this resulted in an interference pattern and made any spectrum acquired useless. This meant that when the system was run at 1 kHz approximately 90% of the spectrum was useful. When the system was run at 10 kHz about 50% of the spectrum was useful and at 20 kHz about 10% of the spectrum was useful. This limited a run speed of 10 kHz because 50% of the spectrum was enough to identify and analyze absorption peaks. This time delay for shut off occurred due to the design of QCLs. Previous research in the near-IR region of the spectrum has not run into this speed limitation due to the switches and boosters used in the near-IR diodes.

3.2 Experiments

3.2.1 Hencken Burner.

The fuel, oxidizer, and nitrogen shroud were piped through an MKS Multigas Controller 647C and then into respective MKS Mass-Flo Controllers. The first step in setting up the Hencken Burner was to determine the calibration on these controllers in order to accurately regulate the mass flow of each gas. For this calibration, a Bios DryCal ML-500 mass flow calibrator was used. For each gas, a flow was entered into the MKS Multigas Controller. The output from the MKS Mass-Flo Controller was piped into the

Bios DryCal which then displayed the actual mass flow of the gas. The results of this calibration are detailed in Figure 3.9.

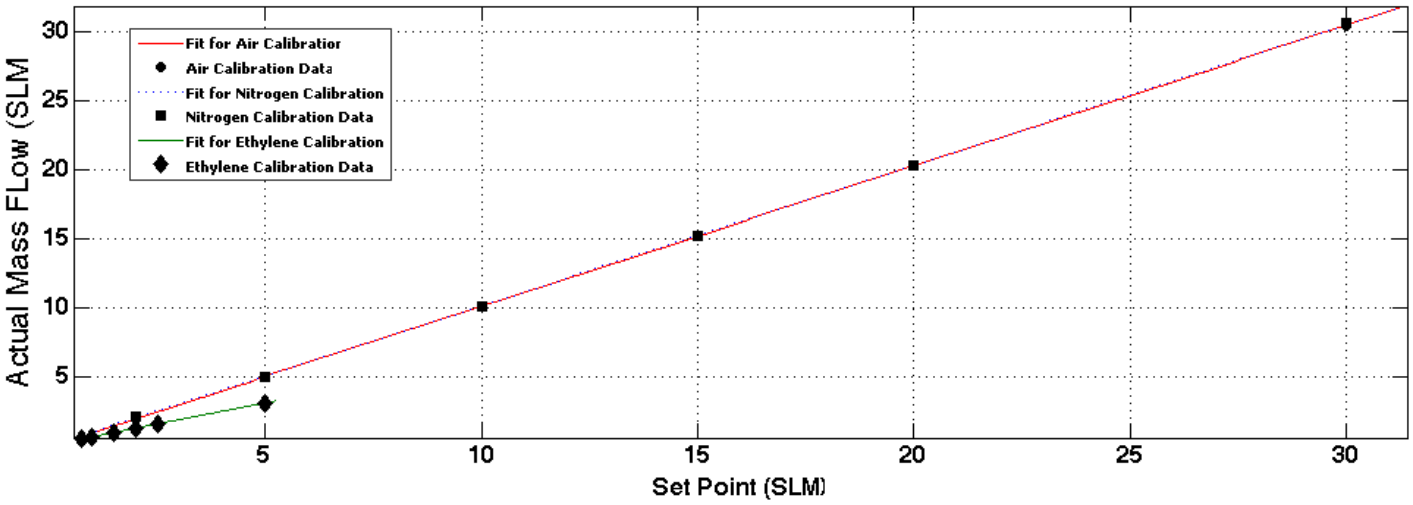

Figure 3.9: The calibration taken from the mass flow controllers. Using this calibration, it was possible to accurately control the equivalence ratio ϕ. Note that the air and nitrogen calibrations sit nearly on top of each other resulting in the "air data" being covered by the "nitrogen data" and the "nitrogen calibration fit" being washed out by the "air calibration fit."

Next, it was necessary to calculate the fuel to air equivalence ratios in terms of mass flow. For this experiment ethylene/air was used first. It was first necessary to calculate the fuel to air ratio under stoichiometric conditions. The stoichiometric chemical equation for burning ethylene in air is

$$C_2H_4 + 3\,O_2 \rightarrow 2\,CO_2 + 2\,H_2O \tag{3.2}$$

Using a mass for air of approximately 29 g/mol and a mass for ethylene of 28 g/mol, yielded a fuel to air (given air is approximately 21% O_2) ratio in stoichiometric conditions of $(\frac{m_{fuel}}{m_{oxidizer}})_{st} = 0.064$. With this number the equivalence ratio could be calculated according

to

$$\phi = \frac{\frac{m_{fuel}}{m_{oxidizer}}}{(\frac{m_{fuel}}{m_{oxidizer}})_{st}} \tag{3.3}$$

Since the mass flow controllers actually output volume flow rates for each gas, it was necessary to expand this equation to

$$\phi = \frac{\frac{\rho_{fuel}\dot{V}_{fuel}}{\rho_{oxidizer}\dot{V}_{oxidizer}}}{(\frac{m_{fuel}}{m_{oxidizer}})_{st}}, \tag{3.4}$$

where ρ is the gas density and $\dot{V}$ is the volume flow rate.

The next step in ensuring an adiabatic flame was to match the flow velocities of the reactants with the flame speed for an ethylene/air flame. The flame speed was a function of the equivalence ratio and was given by,

$$v_f = -4.1747\phi^6 + 30.739\phi^5 - 89.854\phi^4 + 133.37\phi^3 - 107.53\phi^2 + 46.434\phi^2 - 8.2907\phi, \tag{3.5}$$

where ϕ is the equivilance ratio and v_f is the flame velocity [15]. In order to find the speed of the reactants the volumetric flow rate was divided by the cross sectional area from which the reactants were flowing. For a ϕ of one, the flame speed for ethylene was approximately 0.69 m/s according to Equation (3.5). Therefore, the necessary flow rate to match this speed was approximately 25.53 slm for the combined reactants, which corresponded to 24.4 slm for air and 1.13 slm for ethylene for the 1×2 inch Hencken burner used in this experiment. This number is also supported by Meyer et al [18], which used about half the flow rates for a Hencken burner that was half the size. Also, the nitrogen co-flow shroud was velocity matched to the fuel/air flow to avoid any shear layers. This co-flow was changed for each equivalence ratio to ensure accurate results over large equivalence ratio changes. Flow rates for different equivalence ratios are shown in Table 3.1.

With the Hencken working properly and yielding a nearly adiabatic flame temperature, collecting the data was relatively straight forward. Data was taken at 5, 10, 15, 20, and 25 *mm* above the burner. At each height ϕ was varied. First, a data set was taken with

ϕ	Air *slm*	C_2H_4 *slm*	N_2 *slm*
0.5	24.09	1.38	21.74
0.6	24.09	1.66	21.87
0.7	24.09	1.94	22.03
0.8	24.09	2.22	22.18
0.9	24.09	2.5	22.33
1.0	24.09	2.78	22.47
1.1	24.09	3.06	22.62
1.2	24.09	3.34	22.77
1.3	24.09	3.62	22.91
1.4	24.09	3.9	23.06
1.5	24.09	4.18	23.21

Table 3.1: A table detailing the set points for ethylene, air, and nitrogen for the particular mass flow controllers used as well as the Hencken burner

nitrogen purging the entire length of the burner. Then data sets were taken from $\phi = 0.5$ to $\phi = 1.5$, varying ϕ by 0.1 at each step.

Similar procedures were conducted for methane, ethane, and propane. However, it was noted that although the flame speed may be important for low pressure experiments on a Hencken burner without a recessed honeycomb, the Hencken with a recessed honeycomb at atmospheric temperature displayed the best results for all flames at a set flow rate. That is, rather than adjusting the flow rate based upon the flame speed for each fuel, a constant flow rate for air of 24.4 slm was used. The lower density of the gases made the flame speed less important. This resulted in the flame front sitting above the burner enough to minimize heat transfer back to the burner while maintaining a steady, flat, flame front. This result was

qualitatively tested by being able to touch the burner face immediately upon extinguishing the flame after hours of run time. The set points for each fuel, after calibration, are detailed in Tables 3.2, 3.3, 3.4. The flame speed did affect what range of equivalence ratios could be examined. Lower flame speeds resulted in a smaller ϕ sweep. As each fuel became less combustible and had a lower flame speed, the range of equivalence ratios that were measurable became smaller. In order to measure the concentration, a steady flame was needed with no breaks in the flame front over the line of sight measurement. If the flow rates of the fuel and air were too high, the result was an unsteady flame. If the rates were too low there was either no flame at all or a flame that did not cover the burner surface. These conditions resulted in choosing an equivalence ratio sweep of 0.8 to 1.5 for ethane, and 0.75 to 1.25 for methane and propane.

ϕ	Air *slm*	CH_4 *slm*	N_2 *slm*
0.75	24.27	1.728	22.45
0.8	24.27	1.839	22.54
0.85	24.27	1.951	22.63
0.9	24.27	2.063	22.71
0.95	24.27	2.174	22.80
1.0	24.27	2.286	22.89
1.05	24.27	2.398	22.97
1.1	24.27	2.510	23.06
1.15	24.27	2.621	23.15
1.2	24.27	2.733	23.23
1.25	24.27	2.845	23.32

Table 3.2: A table detailing the set points for methane, air, and nitrogen for the particular mass flow controllers used as well as the Hencken burner

ϕ	Air *slm*	C_2H_6 *slm*	N_2 *slm*
0.75	24.27	1.233	22.05
0.8	24.27	1.299	22.10
0.85	24.27	1.365	22.16
0.9	24.27	1.431	22.21
0.95	24.27	1.497	22.27
1.0	24.27	1.562	22.33
1.05	24.27	1.628	22.38
1.1	24.27	21.694	23.44
1.15	24.27	1.760	23.49
1.2	24.27	1.825	23.55
1.25	24.27	1.891	23.60

Table 3.3: A table detailing the set points for ethane, air, and nitrogen for the particular mass flow controllers used as well as the Hencken burner

ϕ	Air *slm*	C_3H_8 *slm*	N_2 *slm*
0.8	24.25	0.768	21.58
0.9	24.25	0.862	21.60
1.0	24.25	0.957	21.65
1.1	24.25	1.051	21.70
1.2	24.25	1.146	21.74
1.3	24.25	1.240	21.79
1.4	24.25	1.335	21.84
1.5	24.25	1.429	21.88

Table 3.4: A table detailing the set points for propane, air, and nitrogen for the particular mass flow controllers used as well as the Hencken burner

IV. Results and Analysis

For each laser and each experimental variation of height and equivalence ratio, 50 measurements were taken at 10 kHz to average out flame effects such as flame flicker as well as any ambient room fluctuations. A representative sample of the data is shown in Figure 4.1. The first step in interpreting the raw data was to use the etalon trace to

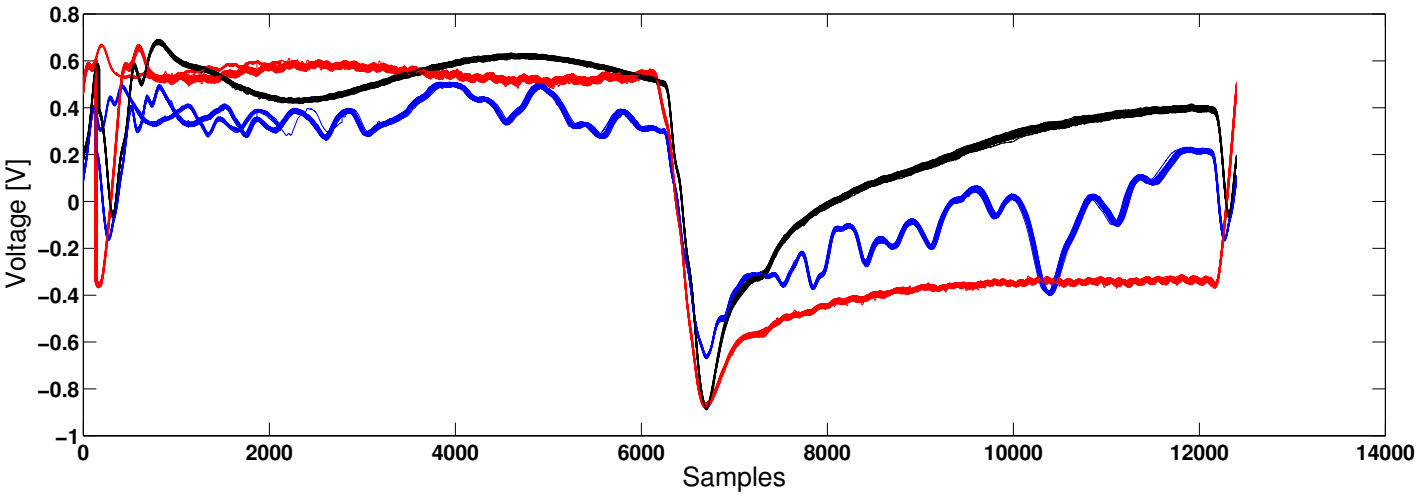

Figure 4.1: (Blue) A representative sample of the 50 raw data samples acquired for an ethylene air flame with an equivalence ratio of 1.0 and height above the burner of 5 mm run at a 10 kHz repetition rate. (Red) A representative sample of the 50 etalon traces under the same conditions. (Black) A representative sample of the the laser intensity with no absorption due to the flame. The CO absorption spectrum corresponds to the left half of the plot and the CO_2 absorption corresponds to the right half.

convert the raw data from a time domain into frequency space. High absorption peaks that do not shift with temperature and pressure are very well known. For relatively abundant molecules, such as CO and CO_2 the fundamental and hot-band transitions have been studied extensively. For these transitions, both analytic calculations and experimental results have found the absorption locations to a very high degree of accuracy. Thus, HITEMP was

assumed to be accurate for the peak locations of these particular molecules. This made it possible to use the center of each peak as the known wavelength for the etalon. With wavelength known at one point, it was then possible to compare the spacing of each etalon peak with the free spectral range in order to convert the absorption profile to frequency space.

With the raw data in frequency space, the Beer-Lambert law was applied in order to express the data in terms of absorption coefficient. This task was accomplished through a four step process. First, the I_0 data was adjusted in the vertical direction. Because there were small effects due to the luminescence of the flame, the data taken with no flame had a slightly lower voltage reading than data with the flame on. This made it necessary to adjust I_0 to match the points where zero absorption occurred. To do this, the minimum absorption was found around the peaks of interest and I_0 was moved to match those minima. This step and the etalon correction are shown in Figure 4.2.

The next step was to adjust the y-axis from voltage space to some sort of absorption space. In absorption space, the zero of the y-axis should correspond to an optically thick concentration. This adjustment is ultimately a simple addition to every data point, and may also be different between data sets due to adjustment of the variable voltage divider. With I_0 properly adjusted and the data properly scaled from voltage space, it was then a simple matter of taking the negative natural logarithm of the quotient of I and I_0 to obtain the Voigt profile of the absorption coefficient as seen in Figure 4.3. It was then possible to find the area under the Voigt profile that was given by the data. This area was in essence the integral of Eq. (2.6); however, this was accomplished numerically with only the data rather than an analytical Voigt profile. In Eq. (2.6), ϕ_ν is a normalized Voigt profile. Therefore, the integral of the Voigt fit to the data will simply be equal to PSX_iL in Eq. (2.2). Now in order to find concentration both the pressure and line strength must be known. The pressure was assumed to be atmospheric pressure in the flame. The line strength is a

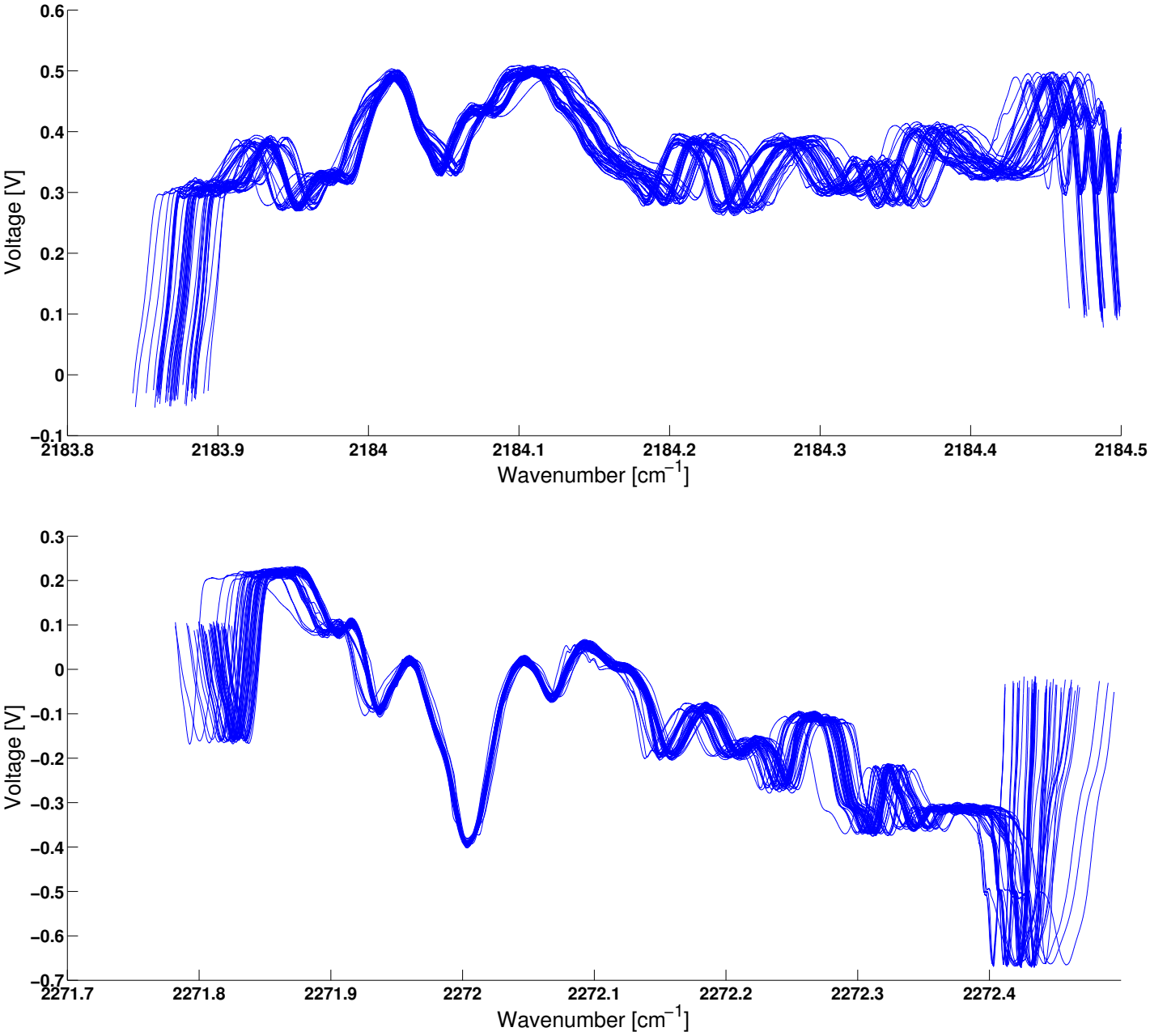

Figure 4.2: (Top) The etalon signal taken on the CO is used to correct the axis using the R(28) as a reference while the etalon from the CO_2 is used for its respective correction using the P(65) as a reference. Using these peaks as reference results in a relatively tight grouping of the 50 data sets in the region of interest while the 50 data sets in each sample tend to diverge away from the points of reference. This data is at an equivalence ratio of 1.0, a height above the burner of 5mm, and a repetition rate of 10 kHz.

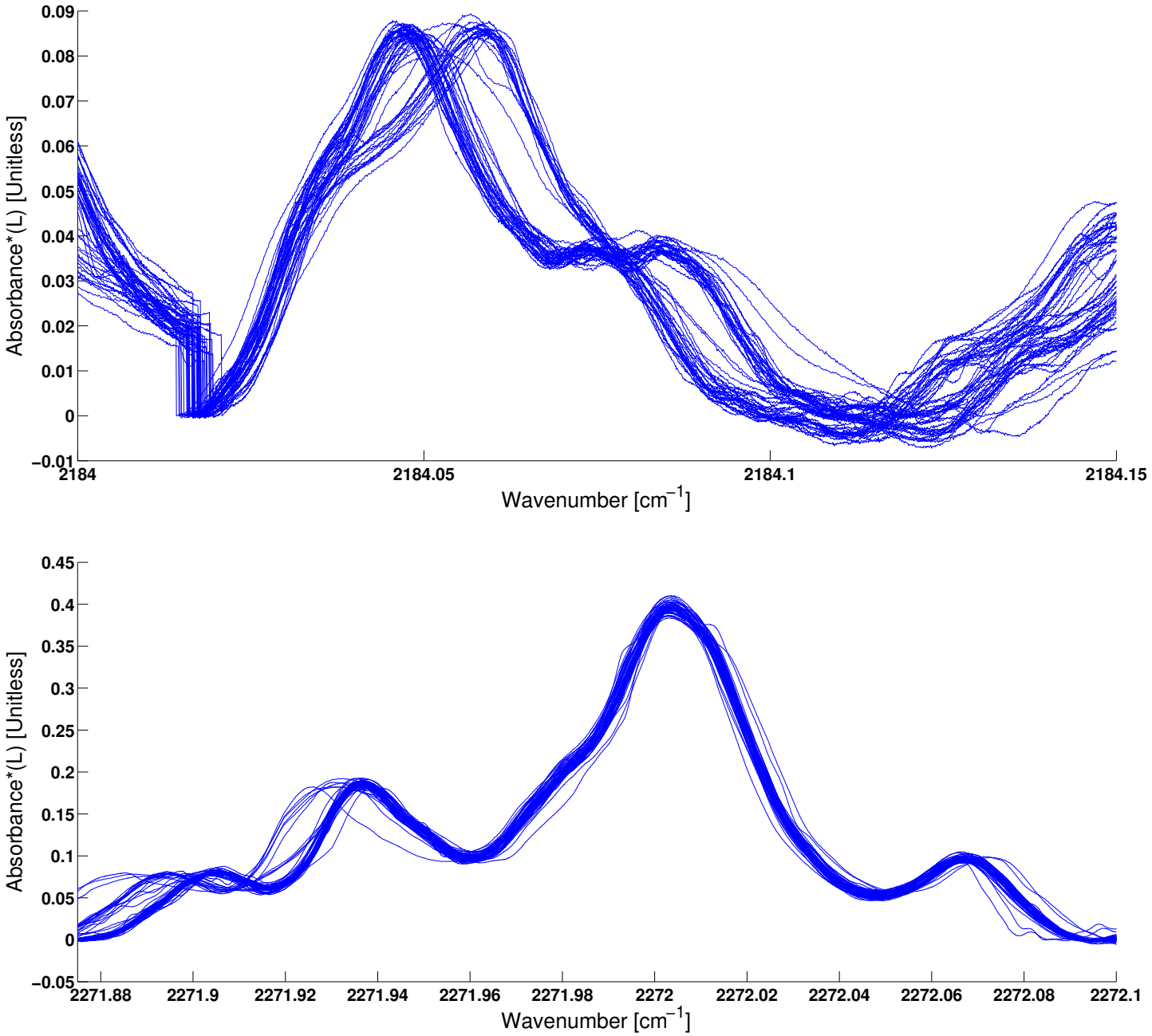

Figure 4.3: In these plots the natural log of $\frac{I}{I_0}$ is taken for both CO (top) and CO_2 (bottom). Concentration for each molecule is found by dividing the area under the region of interest by the pressure, path length, and temperature dependent line strength. This data is at an equivalence ratio of 1.0, a height above the burner of 5mm, and a repetition rate of 10 kHz.

function of temperature, therefore it was necessary to know the temperature. Assuming adiabatic flame temperature across all equivalence ratios yielded decent results; however, previous line of sight measurements have shown greater deviation from adiabatic flame temperature as equivalence ratio is increased [27]. Assuming a variation of 2% to 5% off of adiabatic flame temperature allowed proper scaling on the line strength S, concentration was found by simple division. This method was applied across each of the 50 spectra taken at each experimental variation, and then the results were averaged.

This method of analysis could be applied in simple cases; however, with the CO_2 absorption there were more absorption features near the absorption line of interest. Due to many absorption features being present in this area of the spectrum multiple Voigt profiles must be added together. As was noted before, for the CO molecule a single rovibrational transition was of interest. However, the raw data seen in Figure 4.1, shows a minimum of 5 transitions for CO_2 and in actuality there are more than 10 in the area. Table 4 shows the characteristics of the strongest 7 lines in this region of the spectrum. The integration in

Transition $[J'']$	Wavelength $[nm]$	S 296 K $[\frac{cm^{-1}}{molecule\,cm^{-2}}]$	E" $[cm^{-1}]$
$P(21)$	4401.744	5.06×10^{-21}	4443.88
$P(15)$	4401.666	4.49×10^{-21}	4448.06
$P(4)$	4401.542	1.26×10^{-21}	3926.64
$R(23)$	4401.531	1.08×10^{-21}	5741.45
$P(33)$	4401.414	1.65×10^{-20}	3078.63
$P(65)$	4401.403	6.30×10^{-20}	2394.85
$R(15)$	4401.240	1.08×10^{-21}	5265.09

Table 4.1: A table detailing the 7 strongest absorption features over which the QCL tuned to the CO_2 absorption is scanning over.

this case occurred over all absorption features in the general region of the spectrum. This effectively made the integral of Eq. (2.6),

$$\int k_\nu d\nu = PX_{abs}(S_1(T) + S_2(T) + S_3(T) + ... + S_n(T)) = \int -\frac{\ln \frac{I_L}{I_0}}{L} d\nu, \tag{4.1}$$

where the variables are defined similarly to Eq. (2.6), except each line strength corresponded to the line strength for each absorption line being integrated. Once again, simple algebra from this point allowed for the concentration of the absorption species to be determined.

A similar method of analysis was applied to the CO molecule; however, in this case absorption due to other molecules had to be taken into account. Both CO_2 and H_2O must be considered because at lower equivalence ratios absorption features due to these molecules are of the same order of magnitude as CO absorption as seen in Figure 4.4. Part of the reason for the CO absorption being the same order of magnitude as other transitions was because the actual feature measured was a CO hot band. That is, due to laser limitations, the measured transition was the R(28) v'=4, v"=3 transition. Although it was not ideal to measure a hot band rather than a fundamental transition, the high temperatures in the Hencken burner made measuring the hot band adequate. With multiple species to take into account, the integrated absorbance became,

$$\int k_\nu d\nu = P(X_{CO_2}(S_1(T)+S_2(T)+S_3(T)+...+S_n(T))+X_{H_2O}(S_1(T)+S_2(T)+S_3(T)+...+S_n(T))+X_{CO}S_{CO}(T)). \tag{4.2}$$

The concentration could then be found though algebraic manipulation once again,

$$X_{CO} = \frac{\frac{\int k_\nu d\nu}{PL} - (X_{CO_2}(S_1(T) + S_2(T) + S_3(T) + ... + S_n(T)) + X_{H_2O}(S_1(T) + S_2(T) + S_3(T) + ... + S_n(T)))}{S_{CO}}. \tag{4.3}$$

By applying this method of analysis across all equivalence ratios and all heights it was possible to determine how the molar concentration changed as a function of both

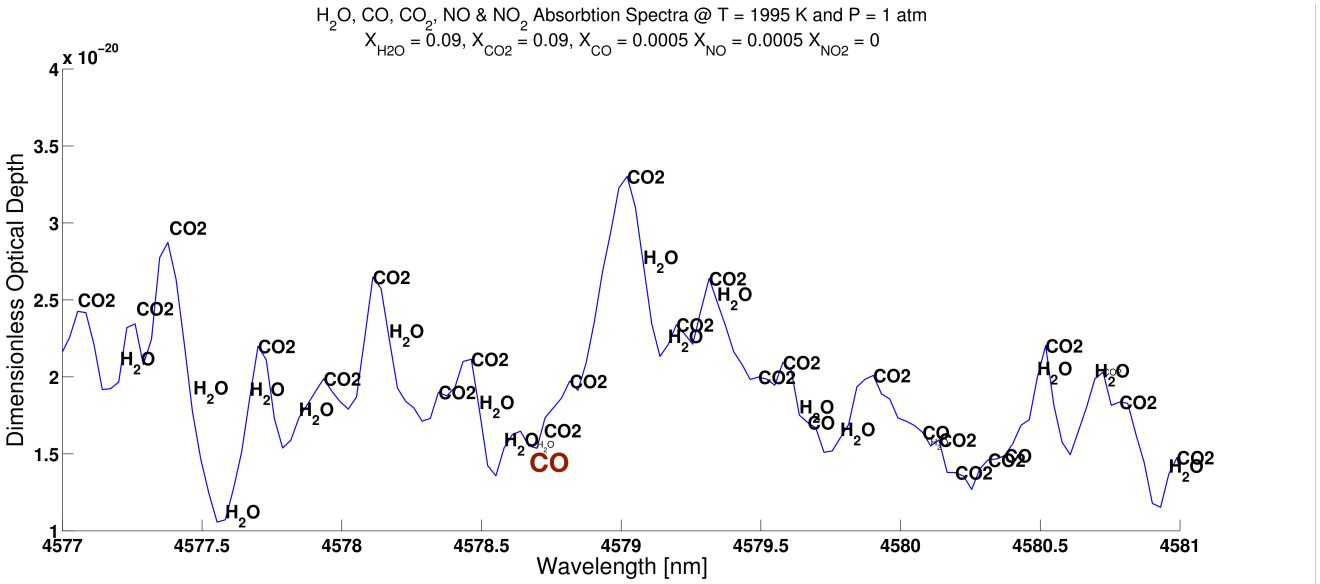

Figure 4.4: A simulation using the HITEMP database showing that at low equivalence ratios absorptions due to CO_2 and H_2O are of the same order of magnitude as the CO R(28), v'=4, v"=3 transition at approximately 4578.7 nm.

equivalence ratio and height as shown in Figure 4.5. Both of these plots show results that are to be expected. When running in lean conditions, as seen in Figure 4.5 (top), almost no CO was produced. This occurred due to the completeness of the reaction. H_2O and CO_2 were the final products to be expected from this reaction. As the fuel air mixture ratio was increased, the reaction became less complete thus producing more CO. Similarly, in an incomplete reaction (in which insufficient oxidizer was present), less CO_2 was present.

Figure 4.5 (bottom) shows how the concentration of each species changes as a function of height for different equivalence ratios for ethylene. As was expected for a calibrated diffusion burner, the data showed that at 5 mm above the flame front the reaction was nearly complete. The small variation in concentration with height was all within the error bounds. For each data set the error could largely be attributed to statistical variation. However, the

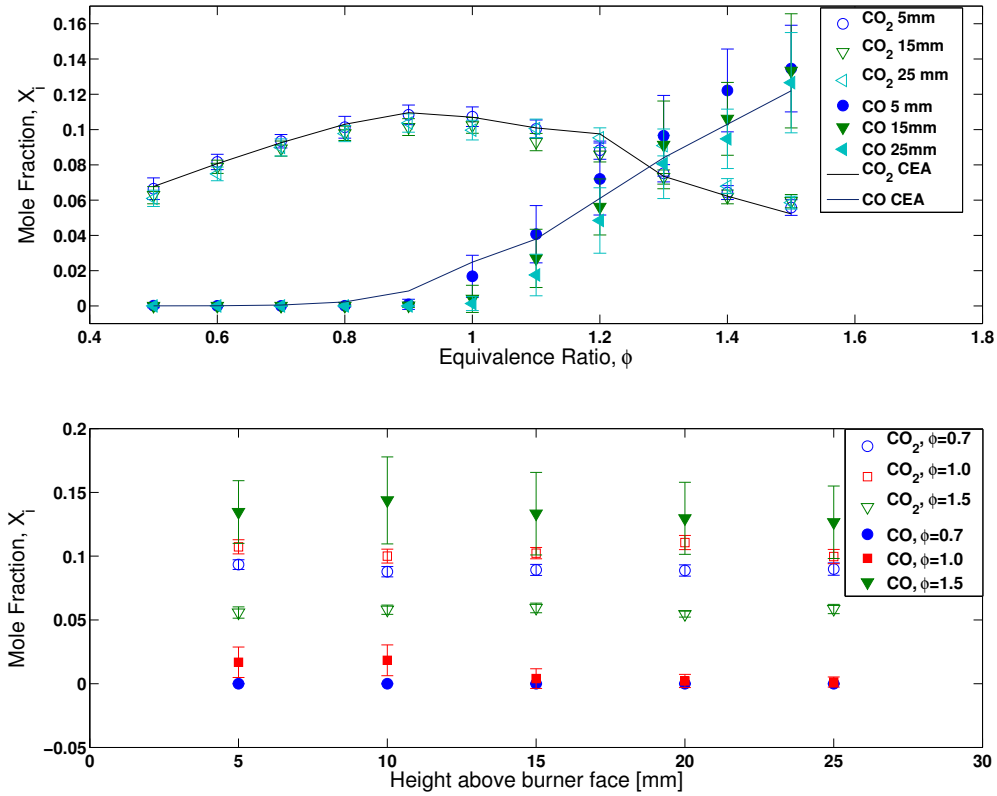

Figure 4.5: (Top) Measured concentration of both CO and CO_2 as a function of equivalence ratio for ethylene. (Bottom) Concentration of CO and CO_2 at various heights. The data in both plots confirms what is expected with less CO_2 and more CO at higher equivalence ratios and nearly constant concentration at the different heights above the burner.

increase in error as height increased showed that there was some error to bulk fluid motion in the flame resulting from expanding boundary layer conditions.

Overall, these effects were minimized by taking data at a 10 kHz repetition rate as well as by using multiple irises near the detector to only allow collimated light into the detector. With the correct concentrations it was possible to find the Combustion Efficiency (CE) according to the equation,

$$CE = \frac{[CO_2]}{[CO_2] + [CO]} \times 100\%. \tag{4.4}$$

Figure 4.6 shows how this value varies with equivalence ratio. Once again this behavior was expected. At lean fuel-air mixtures all fuel underwent combustion, therefore the CE

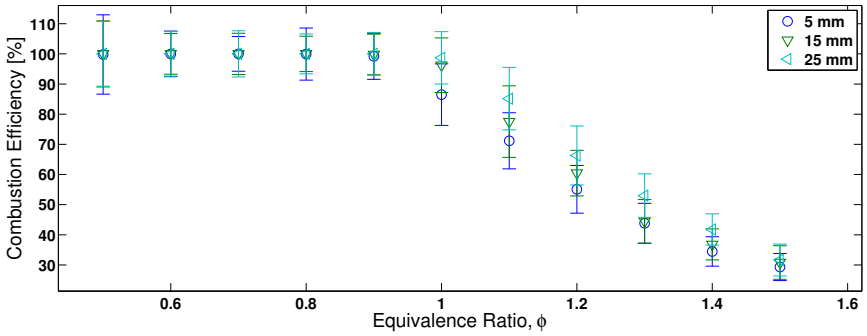

Figure 4.6: Combustion efficiency as a function of equivalence ratio. As the mixture became richer the reaction was less complete which produced more CO. This also showed only a small change in combustion efficiency in the reacting region which is confirmed by Meyer et al.[18]

was very nearly 100%. As more fuel was added, the reaction was less complete due to scarcity of oxidizer, therefore the CE decreased. It is also noteworthy that for the different heights above the burner the CE did not change as can be seen in Figure 4.5 (bottom).

With results collected for ethylene, it was then possible to move on to methane, ethane, and propane, using the exact same method of analysis. The analysis of these fuels is presented in Figures 4.7, 4.8, and 4.9. Once again the results agree with what is expected from Chemical Equilibrium Analysis (CEA) calculations.

Once again the combustion efficiency can be calculated by Equation (4.4). Figure 4.10 shows that as was the case with ethylene, the combustion efficiency could be calculated within 10% uncertainty for methane, ethane, and propane. However, it should be noted that below the detectable limit of CO the combustion efficiency was assumed to be 100%. This assumption is valid to within the error of the experiment. The error in these calculations can be attributed to two major sources, the systematic error and statistical. For the most part the systematic error is largely unquantifiable. It occurs do to discretization of the error, accuracy of fitting the incident intensity to the absorption shoulders, and accuracy of the numerical integration. Out of these errors, only the error due to numerical integration is

easily quantifiable and is a very small contributer to the overall error. On the other hand, the total error is dominated by statistical error due to averaging the concentrations from 50 sweeps over the absorption region. This spread in data occurs due to various fluctuations in the environment that cannot be avoided. Improvement in the error analysis could be improved by quantifying the systematic errors as well as controlling the environment to a higher degree.

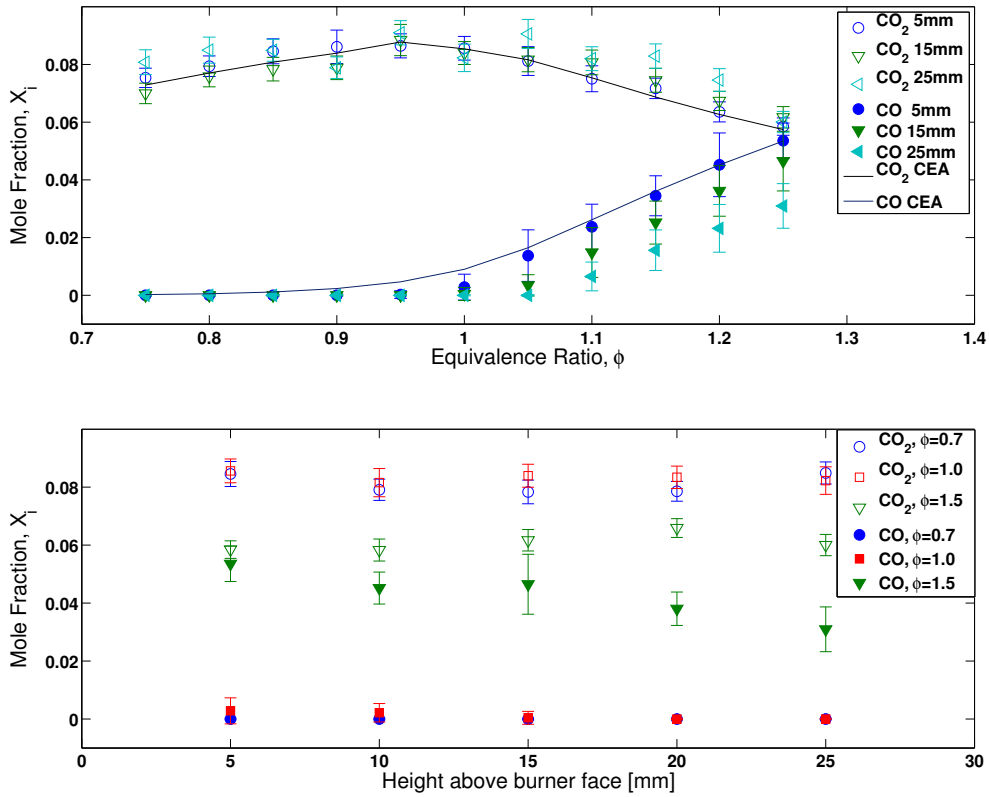

Figure 4.7: (Top) Measured concentration of both CO and CO_2 as a function of equivalence ratio for methane. (Bottom) Concentration of CO and CO_2 at various heights for methane. The data in both plots confirms what is expected with less CO_2 and more CO at higher equivalence ratios and nearly constant concentration at the different heights above the burner. However, due to flame characteristics a much narrower sweep of equivalence ratios was taken.

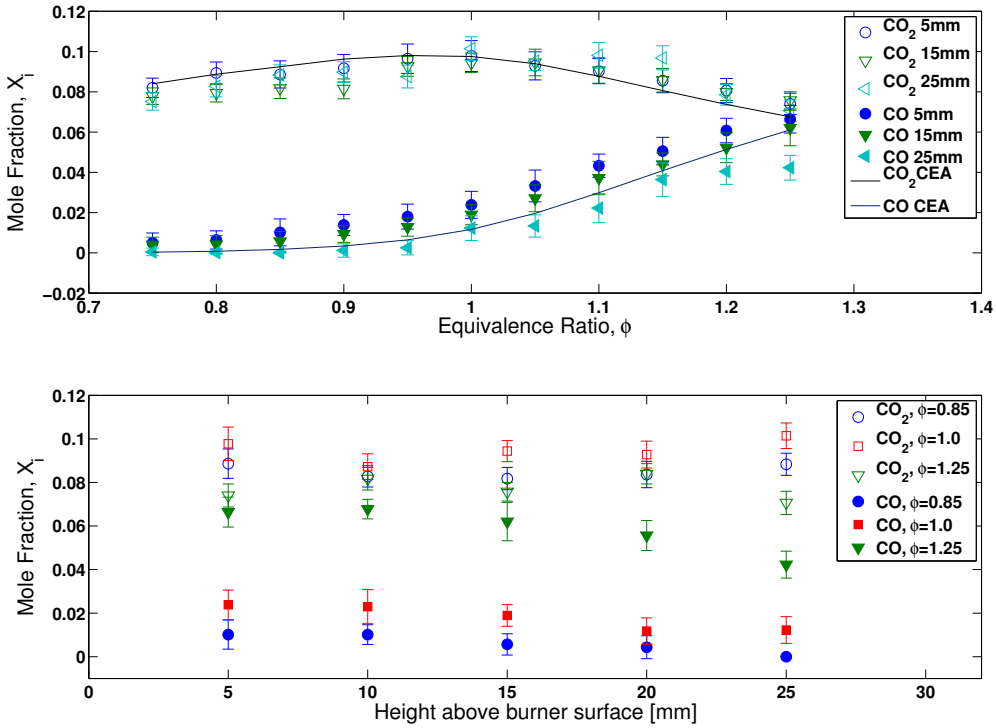

Figure 4.8: (Top) Measured concentration of both CO and CO_2 as a function of equivalence ratio for Ethane. (Bottom) Concentration of CO and CO_2 at various heights for ethane. The data in both plots confirms what is expected with less CO_2 and more CO at higher equivalence ratios and nearly constant concentration at the different heights above the burner. However, due to flame characteristics a much narrower sweep of equivalence ratios was taken.

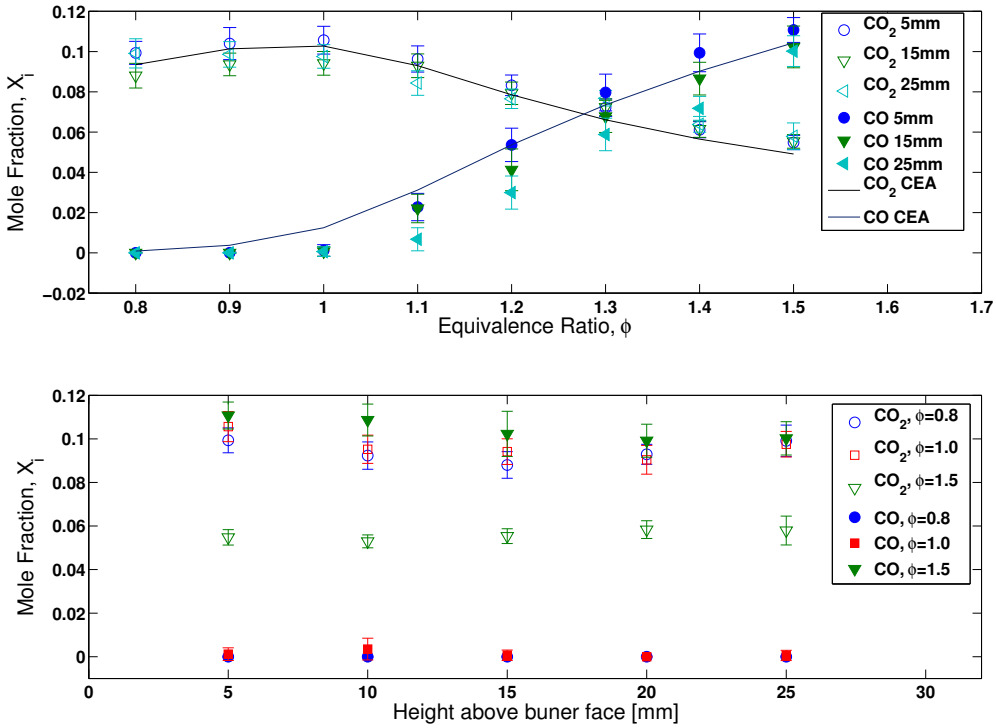

Figure 4.9: (Top) Measured concentration of both CO and CO_2 as a function of equivalence ratio for propane. (Bottom) Concentration of CO and CO_2 at various heights for propane. The data in both plots confirms what is expected with less CO_2 and more CO at higher equivalence ratios and nearly constant concentration at the different heights above the burner. Flame conditions allowed for a wider range of equivalence ratios once again; however, low equivalence ratios would not produce steady flame conditions.

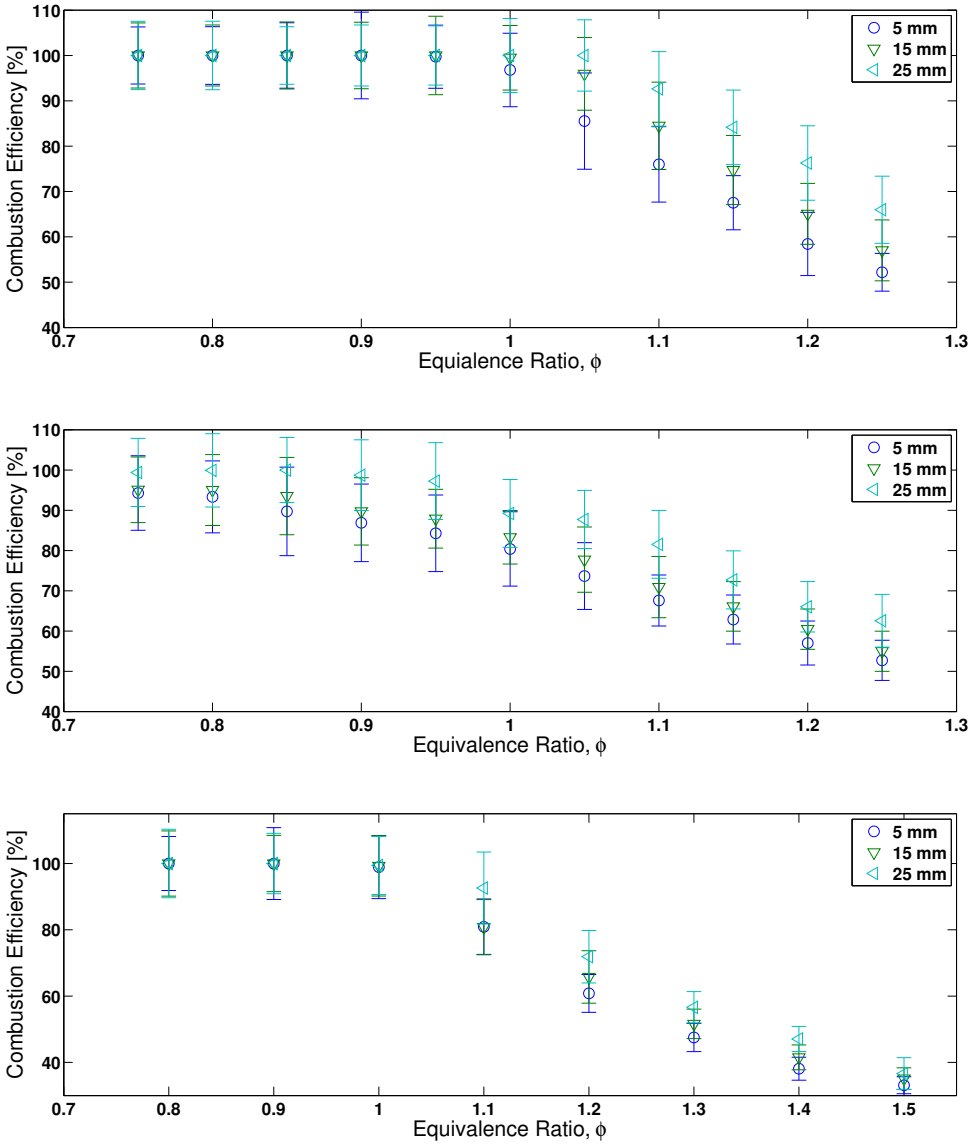

Figure 4.10: The combustion efficiency for methane (top), ethane (middle), and propane (bottom). These results agree with the expected results of efficiency falling off with a rich fuel-air mixture. The results also agree with previous results of very small changes within the reaction region.

V. Conclusions

5.1 Discussion of Findings

Previous TDLAS work, especially in the combustion realm, has been limited to the near-IR region of the spectrum. The measurements that have been taken near 4.5 μm have been done at low repetition rates [3, 20]. This experiment developed and calibrated a mid-IR TDLAS system capable of running at a 10 kHz data collection rate. Utilizing relatively new laser diodes, the R(28) v'=4 to v"=3 hot band absorption was measured for CO and the P(65) fundamental asymmetric stretch absorption was measured for CO_2. This new mid-IR TDLAS system was calibrated by measuring these fundamental absorption lines on a calibrated diffusion burner. The system enabled accurate determination of CO and CO_2 concentration which ultimately led to a determination of combustion efficiency within 10% as a function of equivalence ratio and height for four different fuels. As was expected, combustion efficiency decreases with a more fuel-rich combustion.

5.2 Suggestions for Future Research

Future work with the system will include applying this system to detonation events. The next step in this process will be to fiber-couple the lasers. This should enable the system to be more portable as well as to be used on a variety of devices. To date, InF_3 fiber has been purchased that will be capable of propagating these lasers. Next, broadband collimators need to be purchased in order to fiber couple the system. With the collimators and fiber, it will then be possible to do an analysis on coupling efficiency at these wavelengths. The system must be applied to a pressure cell. The pressure cell will allow for calibration at higher pressures than atmospheric pressure as well as lower pressures. Taking these high and low measurements will allow for more accurate line determination similar to work done by Hanson's group [20]. Although the pressure cell will

not be able to reach the pressures expected in detonation events it will enable a baseline calibration. With the system completely calibrated and transportable, it would then be possible to measure detonation events. The system could measure concentrations of CO and CO_2 in emissions from internal combustion engines, predetonations, shock tubes, Pulse Detonation Engines (PDEs), and Rotary Detonation Engines (RDEs). Furthermore, the original design of having two near-IR lasers as a part of the system can be further explored. This will allow for simultaneous temperature determination by measuring water absorption and employing the two-line technique to acquire temperature data. Finally, further testing of the laser tuned to CO absorption should be further characterized. It should be possible to use this laser to probe a fundamental CO transition. This may reduce the diode lifetime due to driving it at higher temperatures or higher currents. Therefore, a cost-benefit analysis should be completed to determine whether the hot band will provide accurate results or if the fundamental transition is needed.

VI. Appendices

6.1 Representative Plots

The following graphs depict the steps that the matlab code runs through in order to arrive at concentration. Each graph is shown with a low equivalence ratio, a medium equivalence ratio, and a high equivalence ratio. All graphs are for ethylene and air as the combustibles.

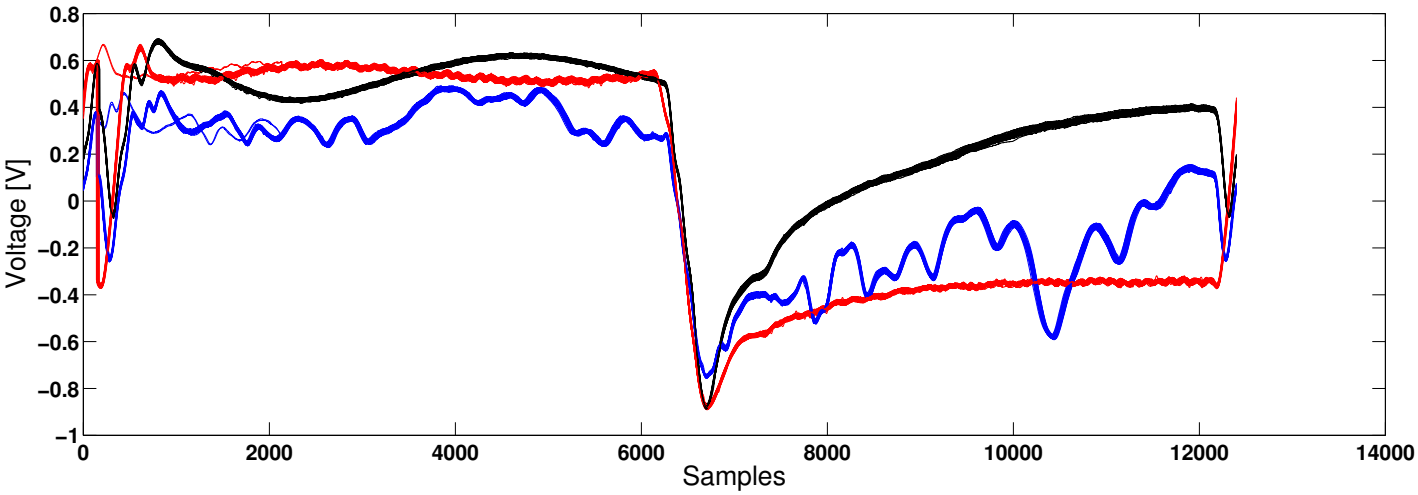

Figure 6.1: (Blue) A representative sample of the 50 raw data samples acquired for an ethylene air flame with an equivalence ratio of 0.7 and height above the burner of 5 mm run at a 10 kHz repetition rate. (Red) A representative sample of the 50 etalon traces under the same conditions. (Black) A representative sample of the the laser intensity with no absorption due to the flame. The CO absorption spectrum corresponds to the left half of the plot and the CO_2 absorption corresponds to the right half.

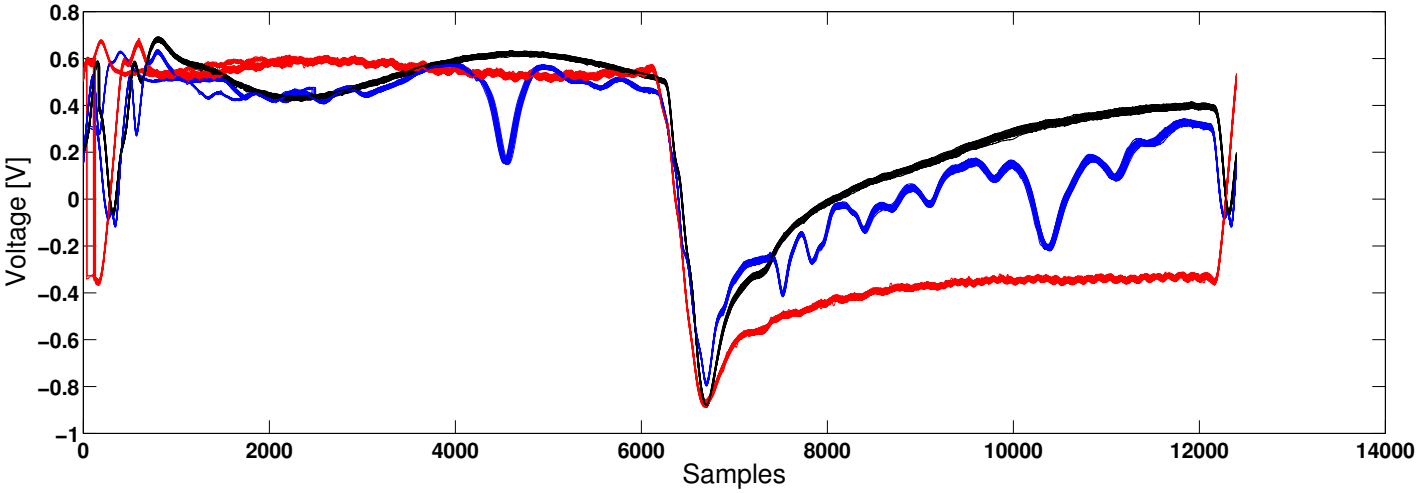

Figure 6.2: (Blue) A representative sample of the 50 raw data samples acquired for an ethylene air flame with an equivalence ratio of 1.5 and height above the burner of 5 mm run at a 10 kHz repetition rate. (Red) A representative sample of the 50 etalon traces under the same conditions. (Black) A representative sample of the the laser intensity with no absorption due to the flame. The CO absorption spectrum corresponds to the left half of the plot and the CO_2 absorption corresponds to the right half.

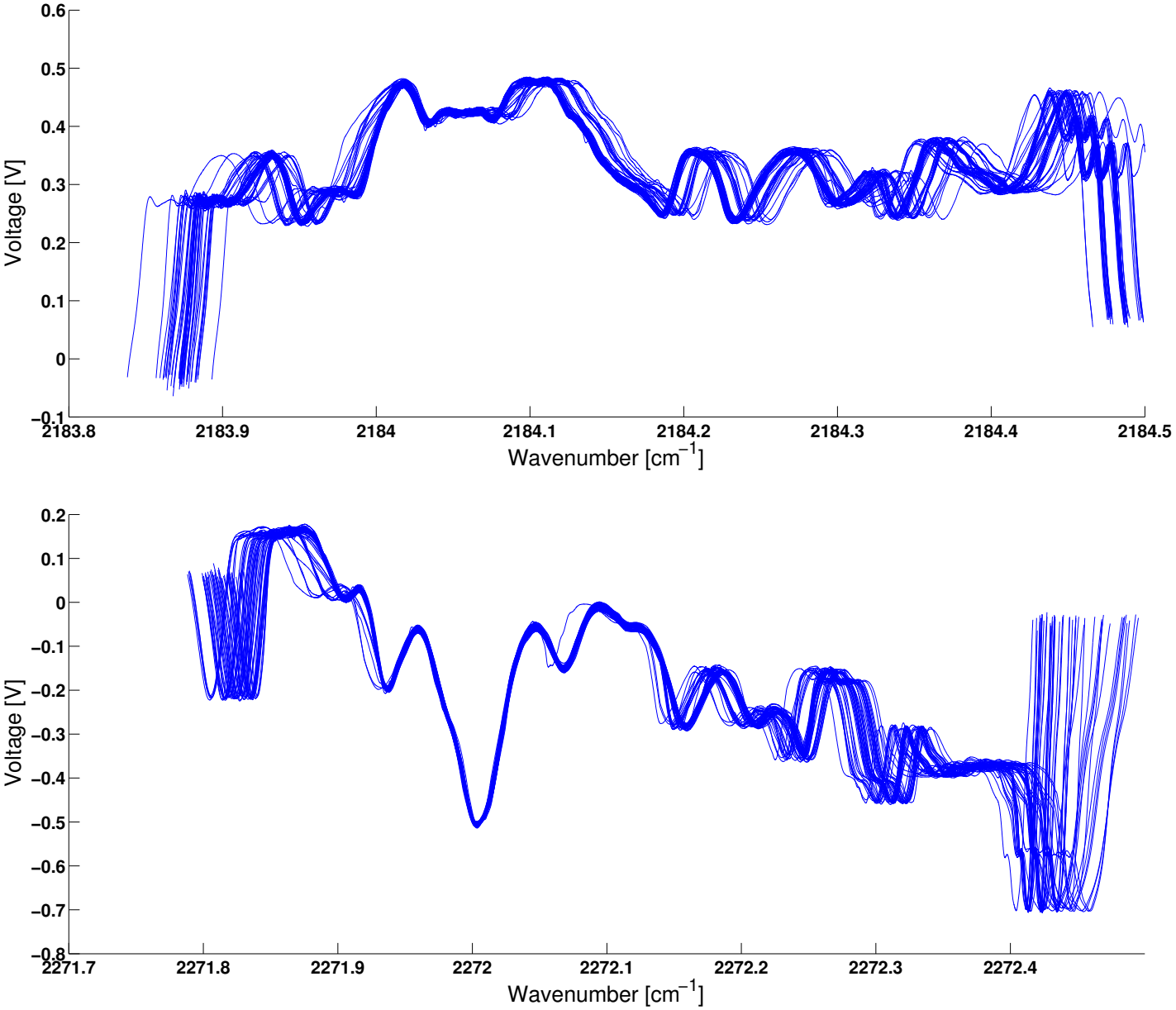

Figure 6.3: (Top) The etalon signal taken on the CO is used to correct the axis using the R(28) as a reference while the etalon from the CO_2 is used for its respective correction using the P(65) as a reference. Using these peaks as reference results in a relatively tight grouping of the 50 data sets in the region of interest while the 50 data sets in each sample tend to diverge away from the points of reference. This data is at an equivalence ratio of 0.7, a height above the burner of 5mm, and a repetition rate of 10 kHz

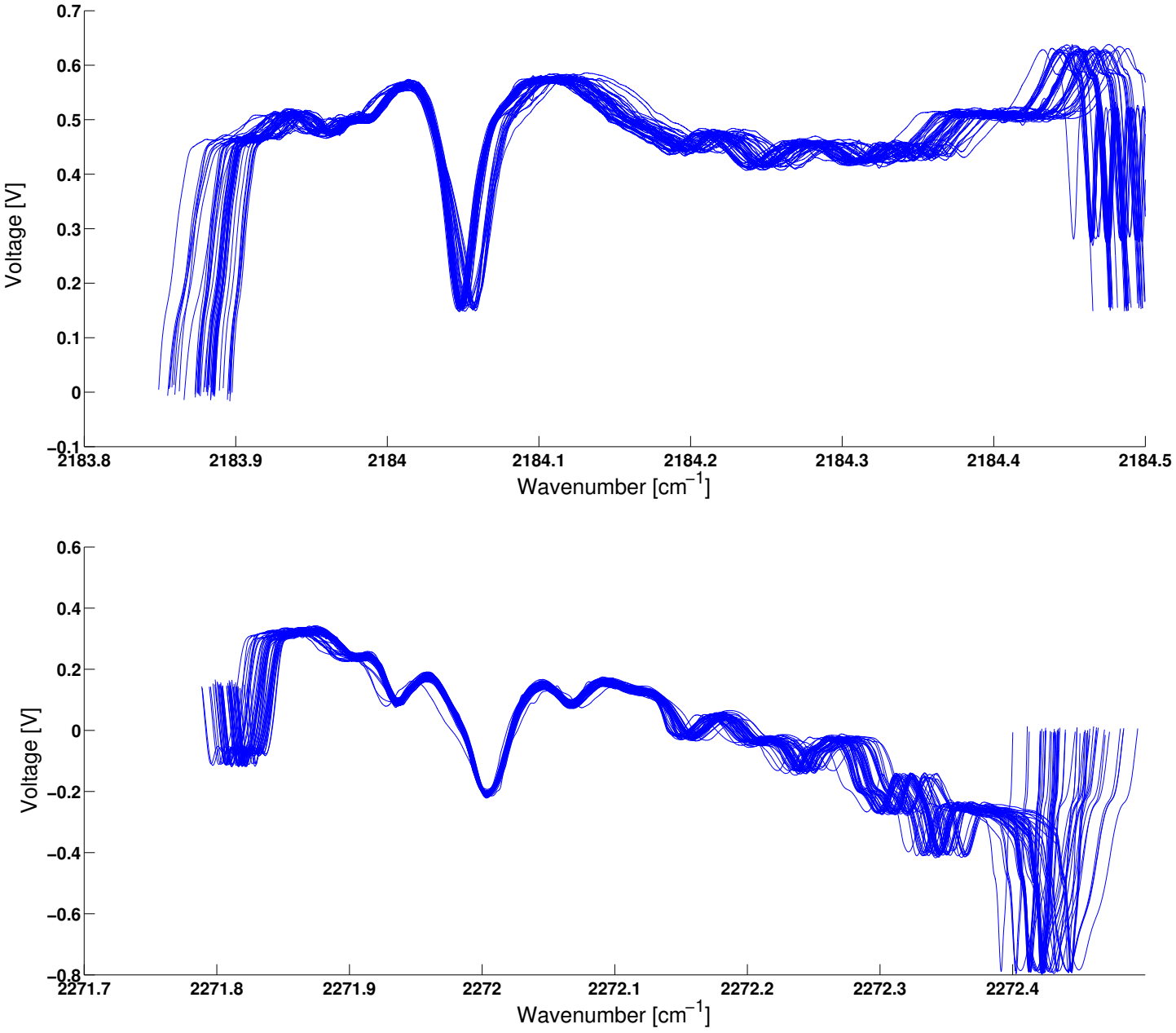

Figure 6.4: (Top) The etalon signal taken on the CO is used to correct the axis using the R(28) as a reference while the etalon from the CO_2 is used for its respective correction using the P(65) as a reference. Using these peaks as reference results in a relatively tight grouping of the 50 data sets in the region of interest while the 50 data sets in each sample tend to diverge away from the points of reference. This data is at an equivalence ratio of 1.5, a height above the burner of 5mm, and a repetition rate of 10 kHz.

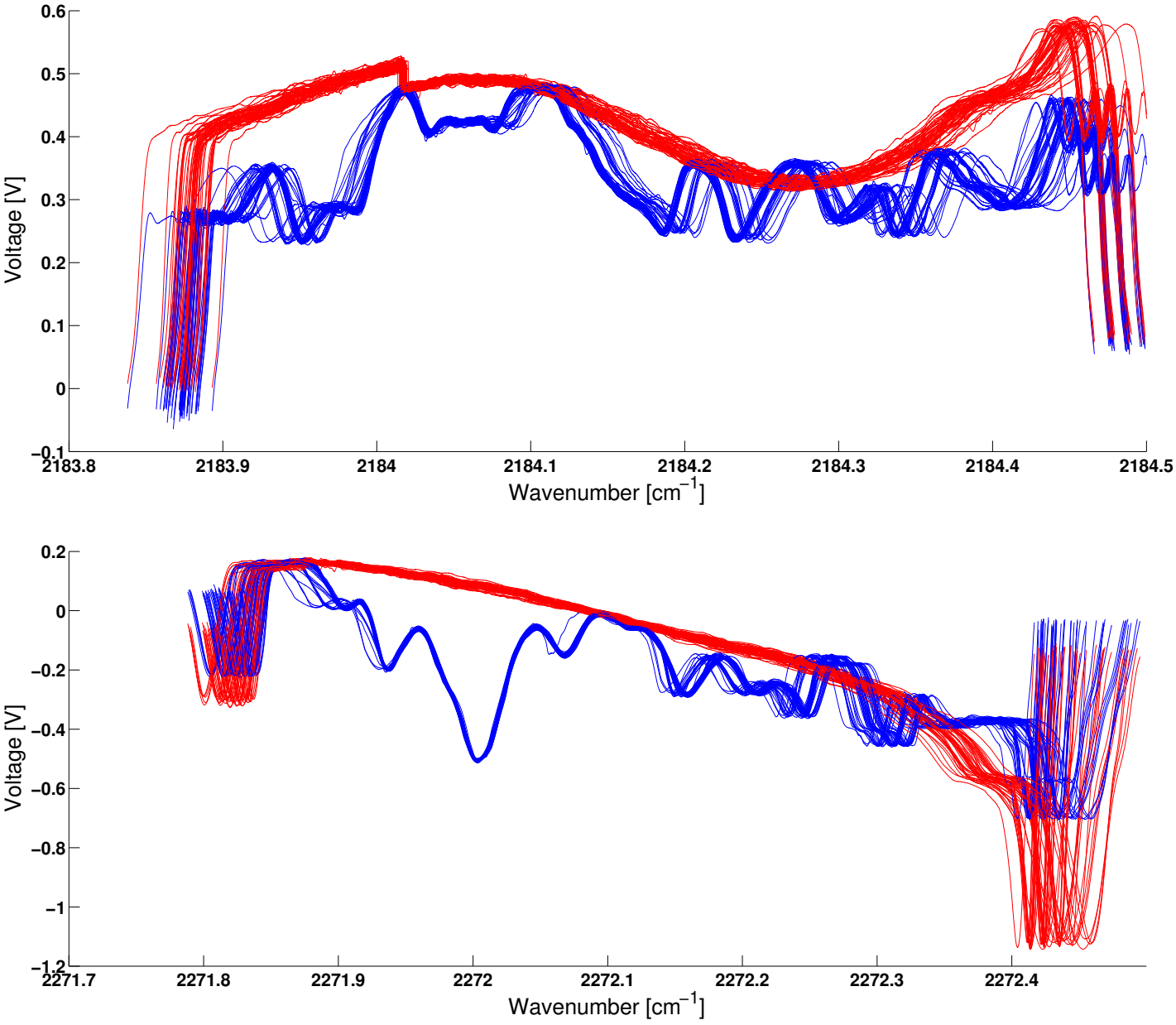

Figure 6.5: Plots showing a properly adjusted "I_0" (red) for both CO (top) and CO_2 (bottom). The red line is the laser intensity with no absorption; however, unlike in the raw data it has been adjusted to line up with zero absorption. That is, the region with no absorption is adjusted vertically to line up with the relative voltage maximums (which correspond to zero absorption) near the peaks of interest. This data is at an equivalence ratio of 0.7, a height above the burner of 5mm, and a repetition rate of 10 kHz.

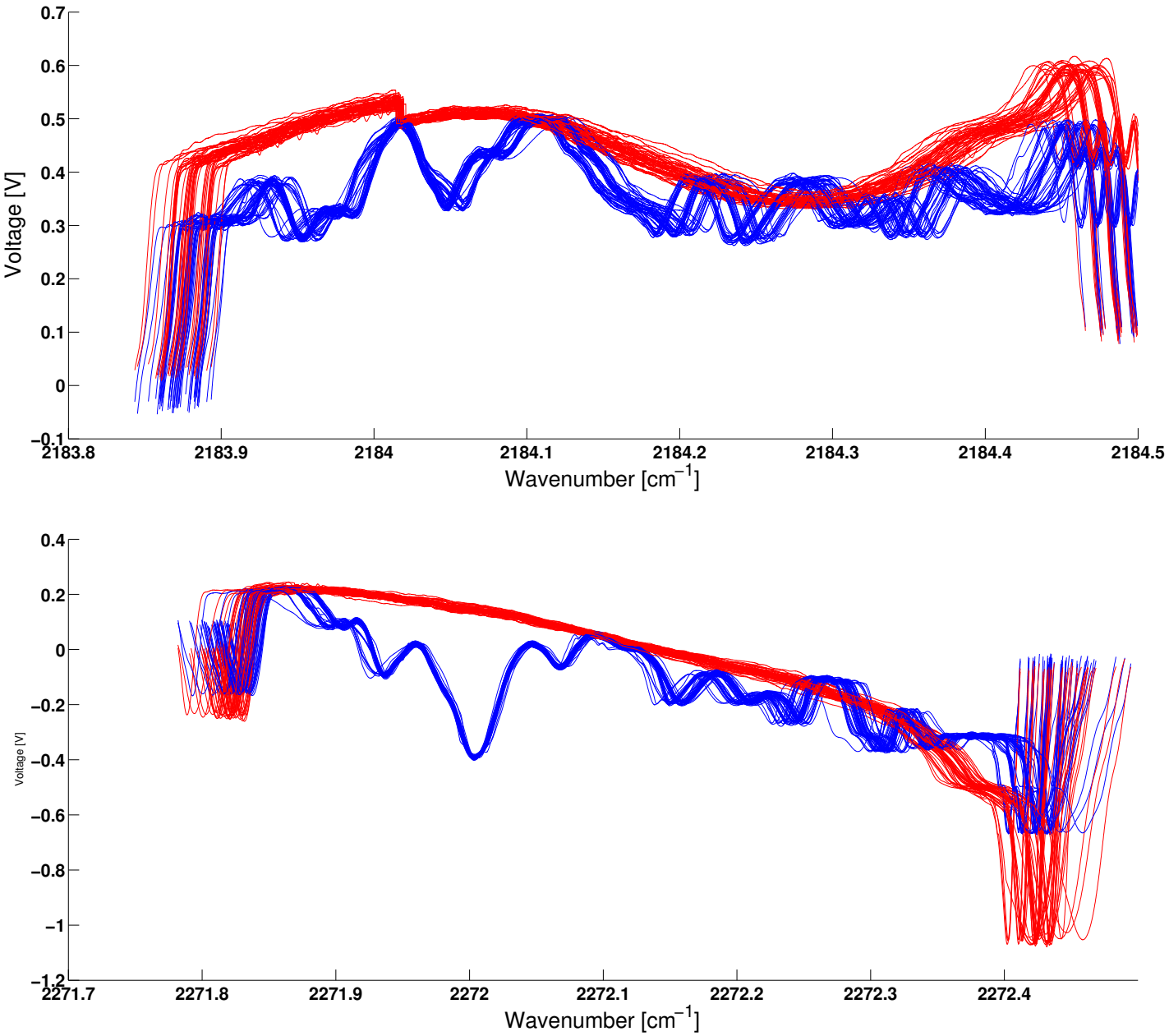

Figure 6.6: Plots showing a properly adjusted "I_0" (red) for both CO (top) and CO_2 (bottom). The red line is the laser intensity with no absorption; however, unlike in the raw data it has been adjusted to line up with zero absorption. That is, the region with no absorption is adjusted vertically to line up with the relative voltage maximums (which correspond to zero absorption) near the peaks of interest. This data is at an equivalence ratio of 1.0, a height above the burner of 5mm, and a repetition rate of 10 kHz.

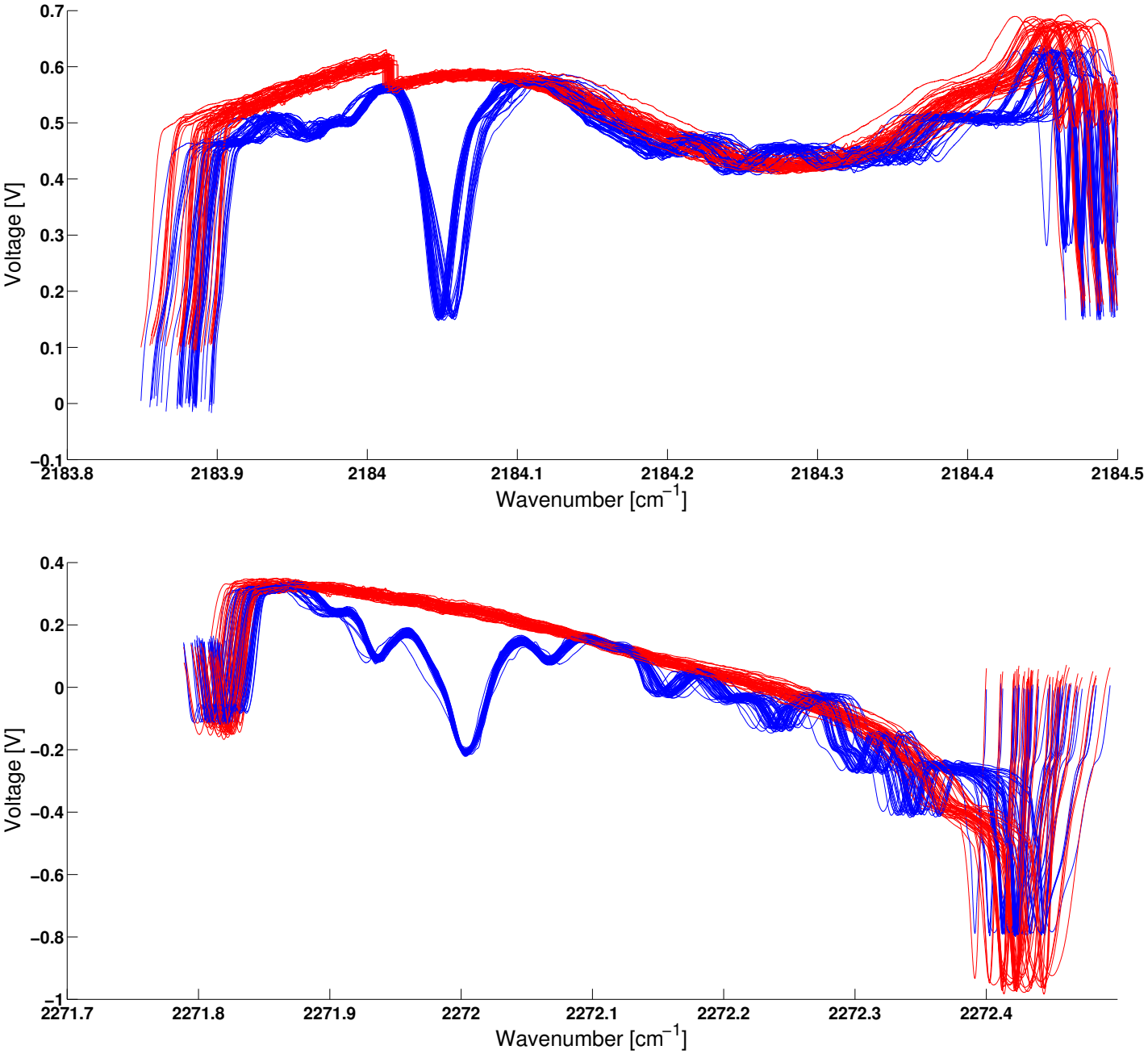

Figure 6.7: Plots showing a properly adjusted "I_0" (red) for both CO (top) and CO_2 (bottom). The red line is the laser intensity with no absorption; however, unlike in the raw data it has been adjusted to line up with zero absorption. That is, the region with no absorption is adjusted vertically to line up with the relative voltage maximums (which correspond to zero absorption) near the peaks of interest. This data is at an equivalence ratio of 1.5, a height above the burner of 5mm, and a repetition rate of 10 kHz.

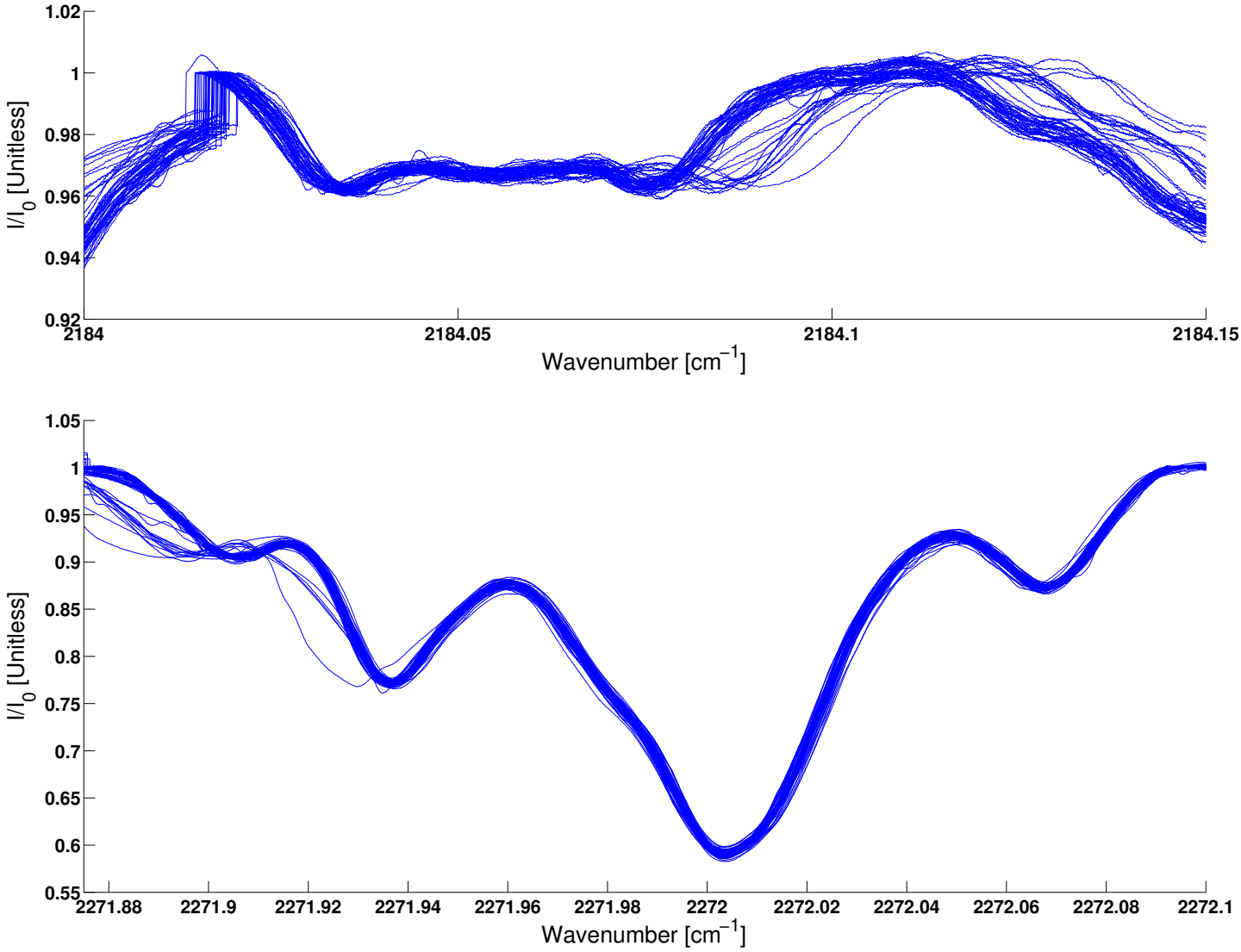

Figure 6.8: Data for CO (top) and CO_2 (bottom) in which the intensity is normalized according to an intensity where no absorption occurs according to Beer's Law. Furthermore, the plots now focus on the regions of interest. For an equivalence ratio of 0.7, height above the burner of 5mm, and repetition rate of 10 kHz, it can be seen that the CO peak is not discernible. It is therefore not detectable and there is more experimental error associated with the 50 data sets in this sample.

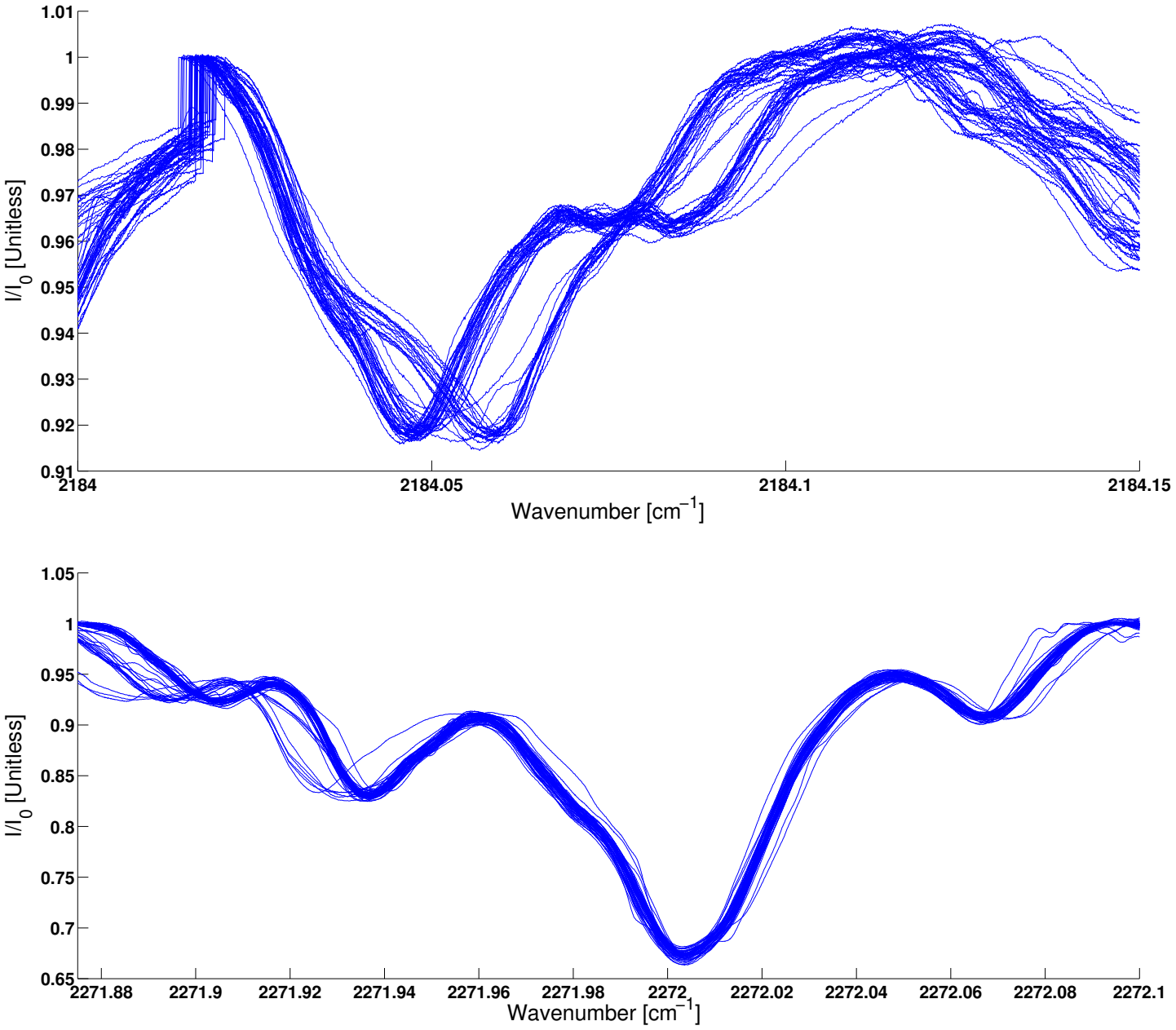

Figure 6.9: Data for CO (top) and CO_2 (bottom) in which the intensity is normalized according to an intensity where no absorption occurs according to Beer's Law. Furthermore, the plots now focus on the regions of interest. For an equivalence ratio of 1.0, height above the burner of 5mm, and repetition rate of 10 kHz, it can be seen that the CO peak is slightly more discernible from nearby features and much more prominent than the low equivalence ratio case. The 50 data sets are much more precise in the region of interest, however due to other absorption features being of the same order of magnitude there is error associated with CO concentrations at this equivalence ratio.

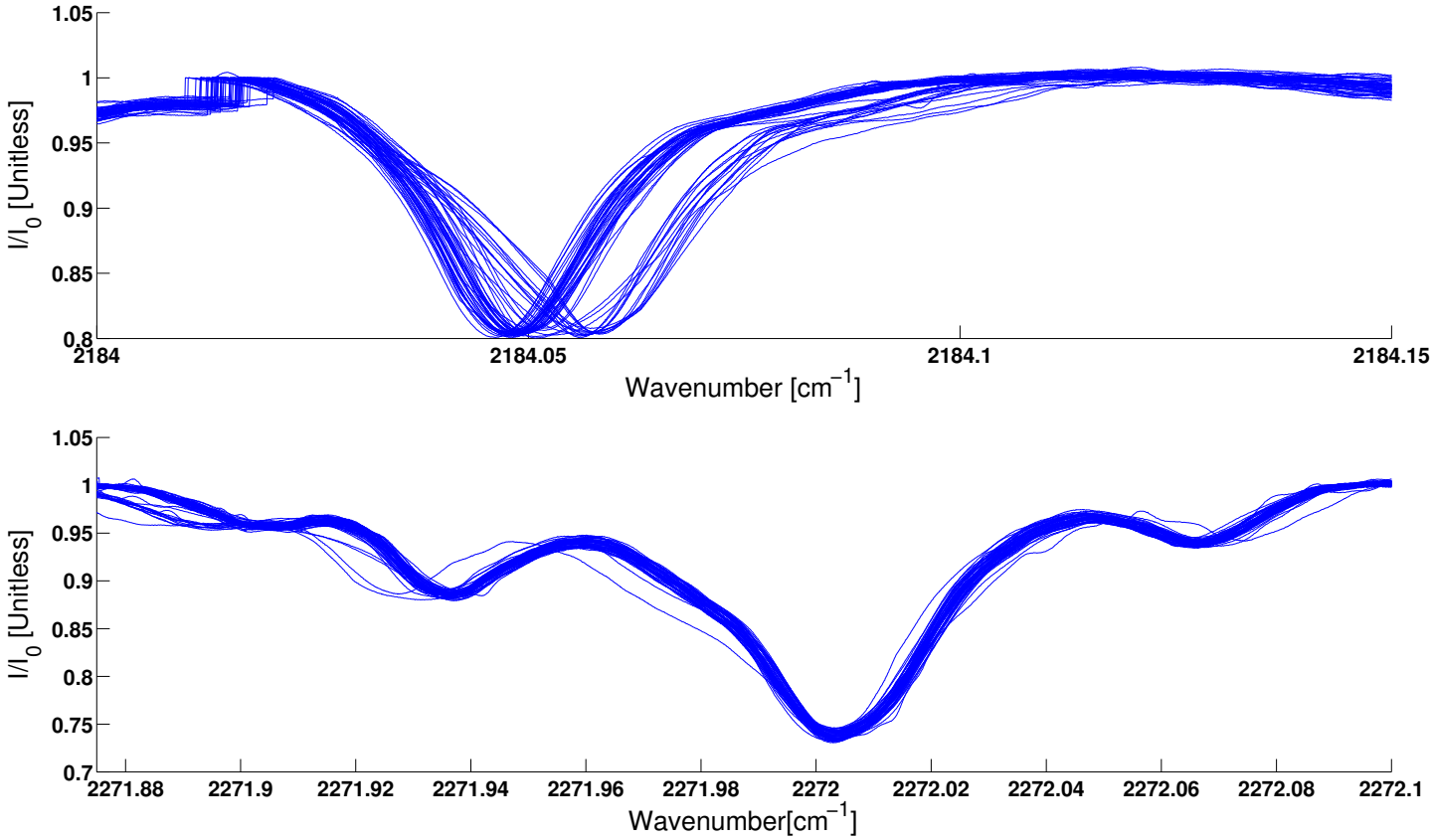

Figure 6.10: Data for CO (top) and CO_2 (bottom) in which the intensity is normalized according to an intensity where no absorption occurs according to Beer's Law. Furthermore, the plots now focus on the regions of interest. For an equivalence ratio of 1.5, height above the burner of 5mm, and repetition rate of 10 kHz, it can be seen that the CO peak is clearly dominating the other features in the area. At this equivalence ratio the 50 data sets are very precise. Therefore, finding CO concentration is possible at higher equivalence ratios.

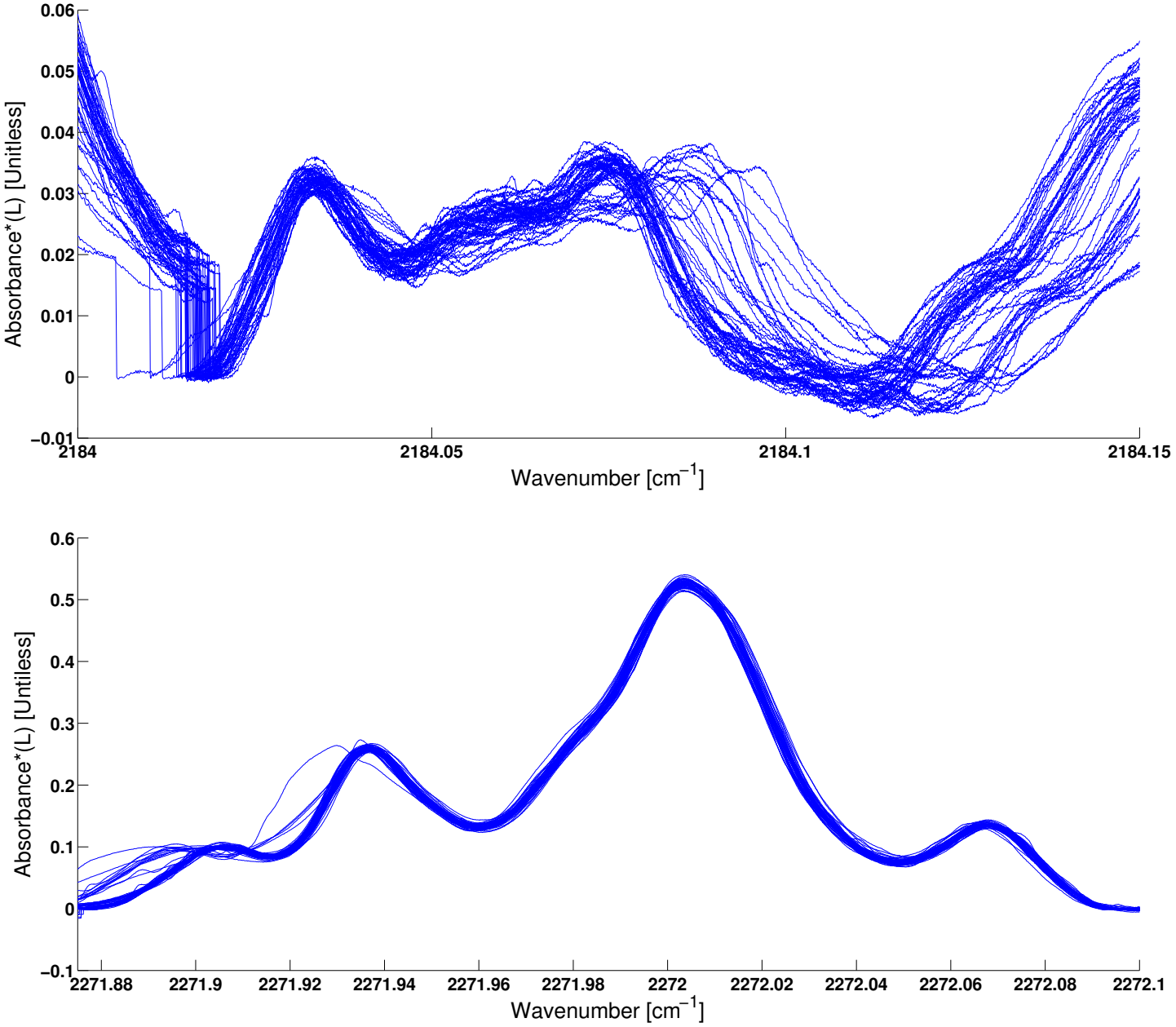

Figure 6.11: In these plots the natural log of $\frac{I}{I_0}$ is taken for both CO (top) and CO_2 (bottom). Concentration for each molecule is found by dividing the area under the region of interest by the pressure, path length, and temperature dependent line strength. This data is at an equivalence ratio of 0.7, a height above the burner of 5mm, and a repetition rate of 10 kHz.

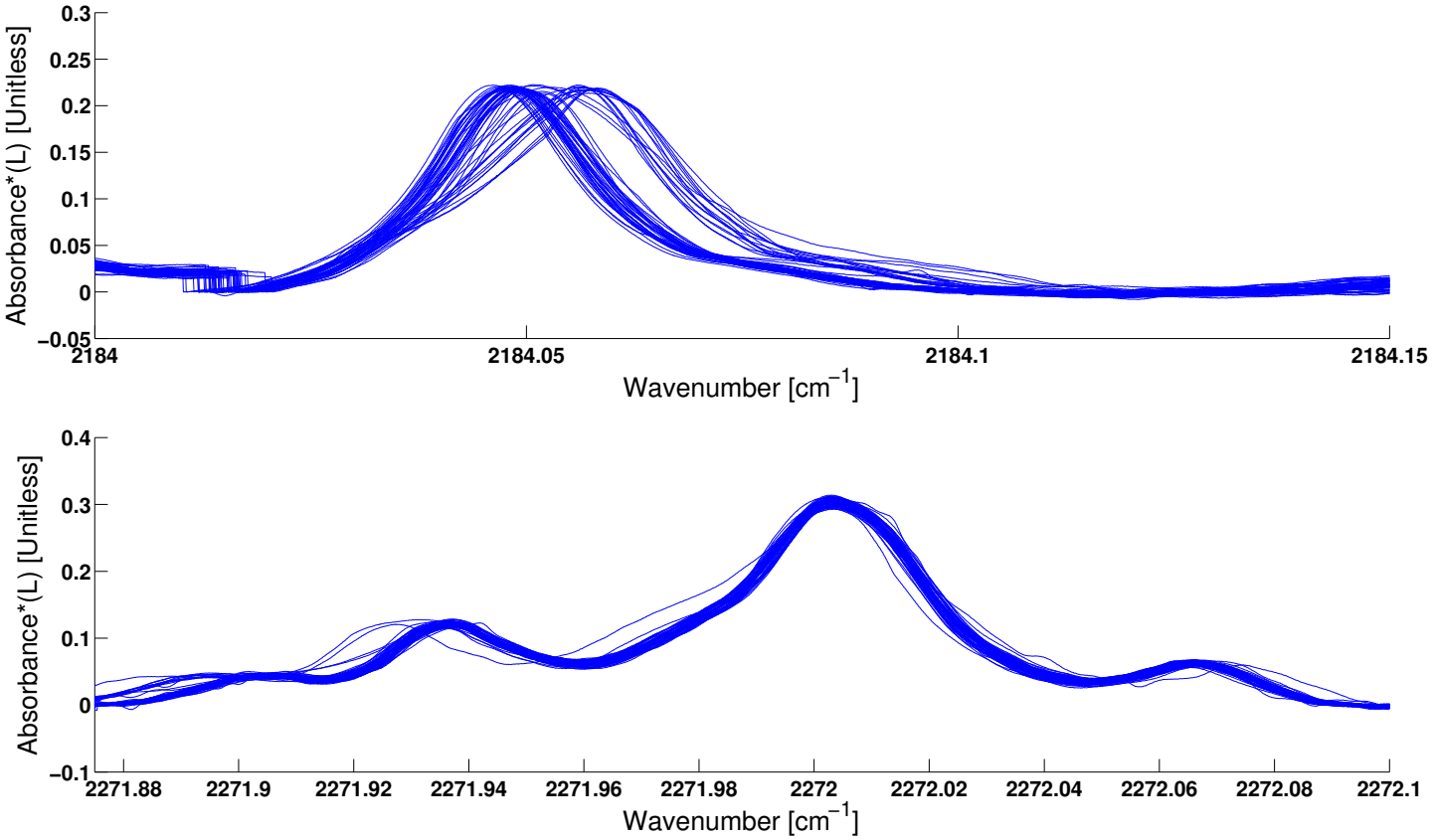

Figure 6.12: In these plots the natural log of $\frac{I}{I_0}$ is taken for both CO (top) and CO_2 (bottom). Concentration for each molecule is found by dividing the area under the region of interest by the pressure, path length, and temperature dependent line strength. This data is at an equivalence ratio of 1.5, a height above the burner of 5mm, and a repetition rate of 10 kHz.

6.2 Code

6.2.1 Main Code.

The following code is the main code shell that reads in the data files

```
function [COAbsorption, COError, CO2Absorption, CO2Error]=TDLAS_Input2
Height = {'5' '10' '15' '20' '25'};  %Various Heights above the burner in mm
for kk=1:size(Height,2)-4
    Fuel=1;  %Fuel selection 1 for ethylene, 2 for methane, 3 for Ethane,
    %4 for propane

    % Different fuels required different equivalence ratios as shown here
    if Fuel==1
        Equivalence={'05' '06' '07' '08' '09' '10' '11' '12' '13' '14' '15'};
        % Ethylene
    elseif Fuel==2 || Fuel==3
        Equivalence={'075' '080' '085' '090' '095' '100' '105' '110' '115'...
            '120' '125'};
    elseif Fuel==4
        Equivalence={'08' '09' '10' '11' '12' '13' '14' '15'};
    end

    for jj=11:size(Equivalence,2);

        %Set up how many data points are taken
        SampRate = 120*10^6;
        SweepRate = 10^7/10^3;
        ScanLength = SampRate/SweepRate;

        Trim_CO = [.001 6]*10^3;
        Trim_CO2 = [.001 6]*10^3;
```

```
27          LengthCO = Trim_CO(2)-Trim_CO(1);
28          LengthCO2 = Trim_CO2(2)-Trim_CO2(1);
29
30          %File Selection
31          if Fuel==1
32              Filename = strcat(...
33                  '/users/stephenwakefield/Desktop/12_06_13/BeamPath_h_',...
34                  Height(kk),'mm.tdms');
35          elseif Fuel==2
36              Filename = strcat(...
37                  '/users/stephenwakefield/Desktop/12_06_13_Methane/BeamPath_h_',...
38                  Height(kk),'mm.tdms');
39          elseif Fuel==3
40              Filename = strcat(...
41                  '/users/stephenwakefield/Desktop/12_17_13_Ethane/BeamPath_h_',...
42                  Height(kk),'mm.tdms');
43          elseif Fuel==4
44              Filename = strcat(...
45                  '/users/stephenwakefield/Desktop/12_17_13_Propane/BeamPath_h_',...
46                  Height(kk),'mm.tdms');
47          end
48
49          %Conversion from national instruments data into something readable in
50          %matlab
51          [ConvertedData,ConvertVer,ChanNames]=convertTDMS(false,Filename);
52          NumScan = (size(ConvertedData.Data.MeasuredData,2)-2)/4;
53
54          %This loop goes through each of the 50 scans and finds the minimum point.
55          %Then it adjusts the data based on that point such that in the raw data CO
56          %is on the left and CO2 is on the right.  This particular loop is without
57          %the flame on
58          for i=1:1:NumScan
```

```
59              Raw{i}.abs_ref = ConvertedData.Data.MeasuredData(2+4*(i-1)+1).Data(401:end);
60              Size=size(Raw{i}.abs_ref,1);
61              [~, Bigptref]=min(Raw{i}.abs_ref);
62              if Bigptref<6300
63                  Bigptref=Bigptref-300+6000;
64              else
65                  Bigptref=Bigptref-300-6000;
66              end
67              RefHolder=zeros(Size,1);
68              RefHolder(1:Size-Bigptref)=Raw{i}.abs_ref(Bigptref+1:Size);
69              RefHolder(Size-(Bigptref-1):Size)=Raw{i}.abs_ref(1:Bigptref);
70              Raw{i}.abs_ref=RefHolder;
71          end
72
73
74          %Temperature and water concentration based off of the fuel used as well as
75          %file selection
76          if Fuel==1
77              Filename = strcat('/users/stephenwakefield/Desktop/12_06_13/phi_',...
78                  Equivalence(jj),'_h_',Height(kk),'mm.tdms');
79              phi = str2num(Equivalence{jj})/10; %Ethylene
80              T = [1599.85; 1806.18; 1995.83; 2161.61; 2289.98; 2368.21; 2390.48;...
81                  2364.16;2312.48; 2252.84; 2191.85];  %%Ethylene
82              T=T-(T.*linspace(.02,.05,11)');
83              T = T(round((phi-0.5)/0.1)+1,1);%Ethylene
84              X_H2O=[.067395; .080101; .092225; .10345; .11342; .12176; .12778;...
85                  .13044;.12957; .12584; .12002];%Ethylene
86              X_H2O = X_H2O(round((phi-0.5)/0.1)+1,1);%Ethylene
87          elseif Fuel==2
88              Filename = strcat('/users/stephenwakefield/Desktop/12_06_13_Methane/phi_',.
89                  Equivalence(jj),'_h_',Height(kk),'mm.tdms');   % Data File
90
```

```
91              phi = str2num(Equivalence{jj})/100; %Methane
92              T = [1918.31; 1995.38; 2067.48; 2132.77; 2187.6; 2224.25; 2230.98; 2208.98;
93                  2174.08; 2135.34; 2095.72]; %% Methane
94              T=T-(T.*linspace(.02,.05,11)');
95              T = T(round((phi-0.75)/0.05)+1,1);%Methane
96              X_H2O =[.14485; .15335; .16156; .16938; .17663; .18286; .18714; .18899;...
97                  .188901; .18778; .18563]; %Methane
98              X_H2O = X_H2O(round((phi-0.75)/0.05)+1,1);
99          elseif Fuel==3
100             Filename = strcat('/users/stephenwakefield/Desktop/12_17_13_Ethane/phi_'...
101                 Equivalence(jj),'_h_',Height(kk),'mm.tdms');    % Data File
102
103             phi = str2num(Equivalence{jj})/100; %Ethane
104             T = [1954.88; 2033.35; 2105.9; 2170.36; 2223.12; 2258.38; 2268.9; 2254.18;.
105                 2224.33; 2188.42; 2150.49]; %% Ethane
106             T=T-(T.*linspace(.02,.05,11)');
107             T = T(round((phi-0.75)/0.05)+1,1);%Ethane
108             X_H2O =[.12525; .13258; .13963; .14632; .15249; .15787; .16195; .16429;...
109                 .16503; .16453; .16307]; %Ethane
110             X_H2O = X_H2O(round((phi-0.75)/0.05)+1,1);
111         elseif Fuel==4
112             Filename = strcat('/users/stephenwakefield/Desktop/12_17_13_Propane/phi_',.
113                 Equivalence(jj),'_h_',Height(kk),'mm.tdms');    % Data File
114
115             phi = str2num(Equivalence{jj})/10; %Propane
116             T = [2040.57; 2177.57; 2264.87; 2262.87; 2198.59; 2122.29; 2045.87;...
117                 1971.38]; %% Propane
118             T=T-(T.*linspace(.0,.05,8)');
119             T = T(round((phi-0.8)/0.1)+1,1);%Propane
120             X_H2O =[.12422; .13708; .14793; .15427; .15489; .15165; .14583; .13832];
121             %Propane
122             X_H2O = X_H2O(round((phi-0.8)/0.1)+1,1);
```

```
123         end
124
125
126         height = str2num(Height{kk});
127
128         P = 1; %Pressure
129
130         close all
131
132         %Use to select file rather than hardcode a file in
133         if exist('Filename','var')==0
134             [Filename,Pathname,FilterIndex] = uigetfile('*.tdms','Select File to Open'),
135             Filename = [Pathname,Filename];
136         end
137
138         [ConvertedData,ConvertVer,ChanNames]=convertTDMS(false,Filename);
139         NumScan = (size(ConvertedData.Data.MeasuredData,2)-2)/4;
140
141
142         for i=1:1:NumScan
143             %This loop goes through each of the 50 scans and finds the minimum point.
144             %Then it adjusts the data based on that point such that in the raw data and
145             %in the etalon data CO is on the left and CO2 is on the right.
146             %This particular loop is with the flame on
147
148             Raw{i}.abs = ConvertedData.Data.MeasuredData(2+4*(i-1)+1).Data(401:end);...
149                 %400 pre-trigger pts
150             Raw{i}.etal = ConvertedData.Data.MeasuredData(2+4*(i-1)+2).Data(401:end);..
151                 %400 pre-trigger pts
152
153             Size=size(Raw{i}.abs,1);
154             [~, Bigpt] = min(Raw{i}.abs);
```

```
155
156             if Bigpt<6300
157                 Bigpt=Bigpt-300+6000;
158             else
159                 Bigpt=Bigpt-300-6000;
160             end
161             Holder=zeros(Size,1);
162             Holder(1:Size-Bigpt)=Raw{i}.abs(Bigpt+1:Size);
163             Holder(Size-(Bigpt-1):Size)=Raw{i}.abs(1:Bigpt);
164             Raw{i}.abs=Holder;
165             Size=size(Raw{i}.etal,1);
166             Holder=zeros(Size,1);
167             Holder(1:Size-Bigpt)=Raw{i}.etal(Bigpt+1:Size);
168             Holder(Size-(Bigpt-1):Size)=Raw{i}.etal(1:Bigpt);
169             Raw{i}.etal=Holder;
170         end
171
172         %Break up CO and CO2 into separate data sets
173         for i=1:1:NumScan
174             Raw{i}.CO = Raw{i}.abs(1:1:Size*1/2);
175             Raw{i}.CO2 =Raw{i}.abs(Size*1/2:1:Size);
176             Raw{i}.CO_etal = Raw{i}.etal(1:1:Size*1/2);
177             Raw{i}.CO2_etal = Raw{i}.etal(Size*1/2:1:Size*1);
178         end
179         clear ConvertedData ConvertVer ChanNames
180         for i=1:1:NumScan
181             Raw{i}.CO = Raw{i}.CO(Trim_CO(1):1:Trim_CO(2));
182             Raw{i}.CO2 = Raw{i}.CO2(Trim_CO2(1):1:Trim_CO2(2));
183             Raw{i}.CO_etal = Raw{i}.CO_etal(Trim_CO(1):1:Trim_CO(2));
184             Raw{i}.CO2_etal = Raw{i}.CO2_etal(Trim_CO2(1):1:Trim_CO2(2));
185         end
186         clear Filename
```

```
187
188
189         for i=1:1:NumScan
190             Raw{i}.CO_ref = Raw{i}.abs_ref(1:1:Size*1/2);
191             Raw{i}.CO2_ref =Raw{i}.abs_ref(Size*1/2:1:Size);
192         end
193         clear ConvertedData ConvertVer ChanNames
194         for i=1:1:NumScan
195             Raw{i}.CO_ref = Raw{i}.CO_ref(Trim_CO(1):1:Trim_CO(2));
196             Raw{i}.CO2_ref = Raw{i}.CO2_ref(Trim_CO2(1):1:Trim_CO2(2));
197         end
198
199
200         %Etalon and reference averaging
201         mean_etal_CO = 0;
202         mean_etal_CO2 = 0;
203         for i=1:1:NumScan
204             mean_etal_CO = mean_etal_CO + Raw{i}.CO_etal;
205             mean_etal_CO2 = mean_etal_CO2 + Raw{i}.CO2_etal;
206         end
207         mean_etal_CO = mean_etal_CO/NumScan;
208         mean_etal_CO2 = mean_etal_CO2/NumScan;
209
210         mean_ref_CO = 0;
211         mean_ref_CO2 = 0;
212         for i=1:1:NumScan
213             mean_ref_CO = mean_ref_CO + Raw{i}.CO_ref;
214             mean_ref_CO2 = mean_ref_CO2 + Raw{i}.CO2_ref;
215         end
216         mean_ref_CO = mean_ref_CO/NumScan;
217         mean_ref_CO2 = mean_ref_CO2/NumScan;
218
```

```
219
220         %Converts x-axis to wavenumber using the etalon data
221         h = waitbar(0,'Processing Etalon Data');
222         for i=1:1:NumScan
223             c = 299732458; % [m/s]
224             d = 0.17; %[m]
225             n = 1.405;
226             Raw{i}.CO2Axis=EtalonAxis(Raw{i}.CO2,Raw{i}.CO2_etal,n,d,2272.003420,3000,.
227                 6000); %(input,etalon input, n,d,wavenumber,general area of peak of
228             %interest)
229             Raw{i}.COAxis=EtalonAxis(Raw{i}.CO,Raw{i}.CO_etal,n,d,2184.0316,4350,4500);
230             waitbar(i/NumScan,h);
231
232         end
233         close(h);
234
235
236         %Adjusts Io properly to fit on top of the absorption of interest
237         h = waitbar(0,'Fitting Io');
238         for i=1:1:NumScan
239             LeftIo=[3300 3700];
240             RightIo = [4400 4700];
241             [Raw{i}.Io_CO] = Find_Io(Raw{i}.CO,Raw{i}.COAxis,LeftIo,RightIo,...
242                 Raw{i}.CO_ref);
243             LeftIo_CO2= [3000 3300];
244             RightIo_CO2= [5300 5700];
245             [Raw{i}.Io_CO2] = Find_Io(Raw{i}.CO2,Raw{i}.CO2Axis,LeftIo_CO2,...
246                 RightIo_CO2,Raw{i}.CO2_ref);
247             waitbar(i/NumScan,h);
248         end
249         close(h);
250
```

```
%divides I by Io, however a conversion from voltage to pure absorption must
%be done.  This is somewhat arbitrary due to the variable voltage divider
%attached to the input signal to adjust the offset.  Essentially the offset
%is taken out so that a signal of 0 corresponds to optically thick
h = waitbar(0,'Normalizing Signal');
for i=1:1:NumScan

    if Fuel==1
        Raw{i}.CO_Norm = (((Raw{i}.CO)+1.6)./((Raw{i}.Io_CO)+1.6));
        Raw{i}.CO2_Norm = (((Raw{i}.CO2)+1.5)./((Raw{i}.Io_CO2)+1.5));
    elseif Fuel==2
        Raw{i}.CO_Norm = (((Raw{i}.CO)+1.50)./((Raw{i}.Io_CO)+1.50));
        Raw{i}.CO2_Norm = (((Raw{i}.CO2)+1.55)./((Raw{i}.Io_CO2)+1.55));
    elseif  Fuel==3
        Raw{i}.CO_Norm = (((Raw{i}.CO)+1.3)./((Raw{i}.Io_CO)+1.3));
        Raw{i}.CO2_Norm = (((Raw{i}.CO2)+1.0)./((Raw{i}.Io_CO2)+1.0));
    elseif Fuel==4
        Raw{i}.CO_Norm = (((Raw{i}.CO)+1.2)./((Raw{i}.Io_CO)+1.2));
        Raw{i}.CO2_Norm = (((Raw{i}.CO2)+1.1)./((Raw{i}.Io_CO2)+1.1));
    end
    waitbar(i/NumScan,h);
end
close(h);

PAR_Data = importdata('parsum.dat',' ',1);%partition function data

%Finds the area under the Voigt profile
h = waitbar(0,'Numerical Integration of Voigt');
for i=1:1:NumScan
    %These find where minimum absorption occurs near the peak of interest.
    %In essence clipping the data to just include the peaks of interest
    [~,pt1]=max(Raw{i}.CO2(LeftIo_CO2(1,1):1:LeftIo_CO2(1,2)));
```

```
283             [~,pt2]=max(Raw{i}.CO2(RightIo_CO2(1,1):1:RightIo_CO2(1,2)));
284             pt1=LeftIo_CO2(1,1)+pt1;
285             pt2=RightIo_CO2(1,1)+pt2;
286             ii_CO2 = [pt1:pt2];
287
288             [~,pt3]=max(Raw{i}.CO(LeftIo(1,1):1:LeftIo(1,2)));
289             [~,pt4]=max(Raw{i}.CO(RightIo(1,1):1:RightIo(1,2)));
290             pt3=LeftIo(1,1)+pt3;
291             pt4=RightIo(1,1)+pt4;
292             ii_CO = [pt3:pt4];
293
294             [Raw{i}.X_CO2,Raw{i}.X_CO2_Err] = Find_Ps_CO2(Raw{i}.CO2_Norm(ii_CO2,1),...
295                 Raw{i}.CO2Axis(ii_CO2,1), 101325, T, PAR_Data);
296             [Raw{i}.X_CO,Raw{i}.X_CO_Err] = Find_Ps(Raw{i}.CO_Norm(ii_CO,1),...
297                 Raw{i}.COAxis(ii_CO,1), 101325, T,4.955E-30,5788.6996,2184.0316,...
298                 PAR_Data,X_H2O,Raw{i}.X_CO2);
299             waitbar(i/NumScan,h);
300         end
301         close(h);
302
303         X_CO = [];
304         X_CO_Err = [];
305         X_CO2 = [];
306         X_CO2_Err = [];
307
308         for i=1:1:NumScan
309             X_CO = [X_CO Raw{i}.X_CO];
310             X_CO_Err = [X_CO_Err Raw{i}.X_CO_Err];
311             X_CO2 = [X_CO2 Raw{i}.X_CO2];
312             X_CO2_Err = [X_CO2_Err Raw{i}.X_CO2_Err];
313         end
314
```

```
315         %Finds average concentrations and associated error.  jj is the equivalence
316         %ratio
317         [muhat,sigmahat,muci,sigmaci] = normfit(X_CO);
318         muhat_Err = sqrt((1/(size(X_CO,2)^2)*sum(X_CO_Err.^2))+2*sigmahat^2);
319         fprintf('CO: %8.7f +/- %8.7f\n',muhat,muhat_Err);
320         Answer1.abs(jj)=muhat;
321         Answer1.err(jj)=muhat_Err;
322         [muhat,sigmahat,muci,sigmaci] = normfit(X_CO2);
323         muhat_Err = sqrt((1/(size(X_CO2,2)^2)*sum(X_CO2_Err.^2))+2*sigmahat^2);
324         fprintf('CO2: %8.7f +/- %8.7f\n',muhat,muhat_Err);
325         Answer.abs(jj)=muhat;
326         Answer.err(jj)=muhat_Err;
327     end
328
329     %stores concentrations and error for all equivalences for a kk height in a matrix
330     COAbsorption(:,kk)=Answer1.abs;
331     COError(:,kk)=Answer1.err;
332     CO2Absorption(:,kk)=Answer.abs;
333     CO2Error(:,kk)=Answer.err;
334 end
```

6.2.2 Axis Correction.

The following code transforms the x-axis from time space (samples) to frequency space (wavenumbers) using the etalon data taken simultaneous to the absorption data.

```
1 function [CorrectedAxis]=EtalonAxis(Sig,EtalSig,n,d,nu,pklow,pkhigh)
2
3 [value, place]=min(Sig(pklow:pkhigh)); %Finds largest absorption peak
4 place=place+pklow;
5
6 [pks, loc] = findpeaks(EtalSig,'minpeakdistance',70); %finds etalon peaks
```

```
[~, inx] = min(abs(loc-place));
loc=loc-min((loc(inx)-place)); %determines distance from etalon peak nearest absorption
loc(loc<=0)=1;

newX_nu=zeros(size(Sig,1),1);



nun=nu;
newX_nu(place)=nun;
if loc(1)==0
    loc(1)=1;
end

%The following loops  start at the etalon peak closest to absorption and
%adjust the x axis based on the the subsequent etalon peaks either forwards
%or backwards.  Units are left in wavenumber for ease of calculation
%(linear spacing).
where=find(loc(:)==place);
for pp=where:-1:2
    FSRnu=.5/(2*n*(d*100));%factor of .5 due to the nature of how the etalon was set up
    newX_nu(loc(pp-1))=nun+FSRnu;
    spacing=(newX_nu(loc(pp))-newX_nu(loc(pp-1)))./(loc(pp)-loc(pp-1));
    for jj = loc(pp-1):loc(pp)
        newX_nu(jj)=newX_nu(loc(pp-1))+spacing*(jj-loc(pp-1));
    end
    nun=newX_nu(loc(pp-1));
end
    for jj = loc(pp-1):-1:1
        newX_nu(jj)=newX_nu(loc(pp-1))+spacing*(jj-loc(pp-1));
    end
```

```
nun=nu;
for pp=where:1:size(loc)-1
    FSRnu=.5/(2*n*(d*100));
    newX_nu(loc(pp+1))=nun-FSRnu;
    spacing=(newX_nu(loc(pp+1))-newX_nu(loc(pp)))./(loc(pp+1)-loc(pp));
    for jj = loc(pp):loc(pp+1)
        newX_nu(jj)=newX_nu(loc(pp))+spacing*(jj-loc(pp));
    end
    nun=newX_nu(loc(pp+1));
end
    for jj = loc(pp+1):size(Sig)
        newX_nu(jj)=newX_nu(loc(pp+1))+spacing*(jj-loc(pp+1));
    end
CorrectedAxis=newX_nu(1:size(Sig));
```

6.2.3 Adjusting I_0.

The following code takes the data taken with no flame present and adjusts it to represent zero absorption.

```
function [Io] = Find_Io(Sig, nu, LeftIo, RightIo,Ref)

%Find the pts with zero absorption
[value1,pt1]=max(Sig(LeftIo(1,1):1:LeftIo(1,2)));
[value1,pt2]=max(Sig(RightIo(1,1):1:RightIo(1,2)));
pt1=LeftIo(1,1)+pt1;
pt2=RightIo(1,1)+pt2;

%The following adusts the reference signal to the zero absorption pts
%around the peak of interest.  The two extremes around the absorption peak
%are adjusted to hit zero absorption exactly, the pts inbetween are
%adjusted by a linear interpolation between the two extremes.
```

```
Total=size(Sig(pt1:pt2));
Average=linspace(0,1,Total(1))';
Average2=zeros(size(Sig,1),1);
Average2(pt1:pt2)=Average;
Io=Ref-((Ref(pt1)-Sig(pt1)).*(1-Average2)+(Ref(pt2)-Sig(pt2)).*(Average2));
```

6.2.4 *Concentration for* CO.

The following code numerically integrates the CO data to find CO concentration.

```
function [X,Err,Vfit,R] = Find_Ps(Sig,nu,P,T,S_ref, E,nu_line,PAR_Data,X_H2O,X_CO2);

global nu_start nu_end

%defines beginning and end of signal
nu = nu(1:10:end);
nu_start = nu(end);
nu_end = nu(1);

%Take the natural log according to Beer's law and reduce data by 10 for
%ease of computing
Sig = -log(Sig);
Sig = Sig(1:10:end);


P = P/101325;%Pressure to atm

A = trapz(nu(end:-1:1),Sig); %numeric integration of Voigt profile

%Setup partition function and linestrength
Q_T_Ref = Q(296,5,1,PAR_Data);
Q_T = Q(T,5,1,PAR_Data);
```

```
c2 = 1.4388;    % [cm K]
S = S_ref*Q_T_Ref/Q_T*(296/T)*exp(-c2*E/T)/exp(-c2*E/296)*(1-exp(-c2*nu_line/T))/...
    (1-exp(-c2*nu_line/296));


%load in HITEMP data in the region of the spectrum of interest
load('HITEMP.mat');
Lines=HITEMP(find(HITEMP(:,3)>nu_start,1,'first'):find(HITEMP(:,3)<nu_end,1,'last'),:);

%Calculate partition function for CO2 and H2O
Q_T_Ref_CO2 = Q(296,2,1,PAR_Data);
Q_T_CO2 = Q(T,2,1,PAR_Data);
Q_T_Ref_H2O = Q(296,1,1,PAR_Data);
Q_T_H2O = Q(T,1,1,PAR_Data);


%Get line strengths for CO2 and H2O in the area of interest
S_H2O=0;
S_CO2=0;
for ii=1:size(Lines,1);
if Lines(ii,1)==2 && Lines(ii,2)==1
S_CO2 = S_CO2 + Lines(ii,4)*Q_T_Ref_CO2/Q_T_CO2*(296/T)*exp(-c2*Lines(ii,8)/T)/...
    exp(-c2*Lines(ii,8)/296)*(1-exp(-c2*Lines(ii,3)/T))/(1-exp(-c2*Lines(ii,3)/296));
elseif Lines(ii,1)==1 && Lines(ii,2)==1
S_H2O = S_H2O + Lines(ii,4)*Q_T_Ref_H2O/Q_T_H2O*(296/T)*exp(-c2*Lines(ii,8)/T)/...
    exp(-c2*Lines(ii,8)/296)*(1-exp(-c2*Lines(ii,3)/T))/(1-exp(-c2*Lines(ii,3)/296));
end
end


X_CO2=X_CO2-X_CO2*.3; %Calibration factor applied accross all fuels
%Calculate concentration
```

```
55 if (((A)/(2*2.54*P))-((S_H2O*7.338933E21/T)*X_H2O)-((S_CO2*7.338933E21/T)*X_CO2))<0
56     %i.e. not detectable
57     X=0; %A negative concentration doesn't make sense and causes graphs to look
58     %incorrect
59 else
60 X=(((A)/(2*2.54*P))-((S_H2O*7.338933E21/T)*X_H2O)-((S_CO2*7.338933E21/T)*X_CO2))/...
61     (S*7.338933E21/T);
62 end
63 %determine error
64 dSig=diff(Sig);
65 dnu=diff(nu);
66 firstderiv=dSig./dnu(end:-1:1);
67 Maxerr=max(diff(firstderiv)./dnu(end:-1:2));
68 Err =Maxerr.*((nu(end)-nu(1))/(12*size(nu,1).^2));
69
70
71 %Determine the partition function for specific molecules and isotopes
72 function [par] = Q(T,Mol,Iso,PAR_Data);
73
74 if Mol==1
75     if Iso==1
76         ind=2;
77     elseif Iso==2
78         ind=3;
79     elseif Iso==3
80         ind=4;
81     elseif Iso==4
82         ind=5;
83     elseif Iso==5
84         ind=6;
85     elseif Iso==6
86         ind=7;
```

```
87      end
88  elseif Mol==2
89      if Iso==1
90          ind=1+7;
91      elseif Iso==2
92          ind=2+7;
93      elseif Iso==3
94          ind=3+7;
95      elseif Iso==4
96          ind=4+7;
97      elseif Iso==5
98          ind=5+7;
99      elseif Iso==6
100         ind=6+7;
101     elseif Iso==7
102         ind=7+7;
103     elseif Iso==8
104         ind=8+7;
105     end
106 elseif Mol==5
107     if Iso==1
108         ind=39;
109     elseif Iso==2
110         ind=40;
111     elseif Iso==3
112         ind=41;
113     elseif Iso==4
114         ind=42;
115     elseif Iso==5
116         ind=43;
117     elseif Iso==6
118         ind=44;
```

```
    end
elseif Mol==8
    if Iso==1
        ind=51;
    elseif Iso==2
        ind=52;
    elseif Iso==3
        ind=53;
    end
elseif Mol==10
    if Iso==1
        ind=56;
    end
end

par = interp1(PAR_Data.data(:,1),PAR_Data.data(:,ind),T);
```

6.2.5 Concentration for CO_2.

THE following code numerically integrates the CO_2 data to find CO_2 concentration.

```
function [X,Err,Vfit,R] = Find_Ps_CO2(Sig,nu, P, T, PAR_Data);

global nu_start nu_end

%defines beginning and end of signal
nu = nu(1:10:end);
nu_start = nu(end);
nu_end = nu(1);

%Take the natural log according to Beer's law and reduce data by 10 for
%ease of computing
```

```
Sig = -log(Sig);
Sig = Sig(1:10:end);
P = P/101325;


%load in HITEMP data in the region of the spectrum of interest
 load('New');
S_ref=New(find(New(:,2)>nu_start,1,'first'):find(New(:,2)<nu_end,1,'last'),3);
nu_line=New(find(New(:,2)>nu_start,1,'first'):find(New(:,2)<nu_end,1,'last'),2);
E=New(find(New(:,2)>nu_start,1,'first'):find(New(:,2)<nu_end,1,'last'),7);

%Numerically integrate the signal
A = trapz(nu(end:-1:1),Sig);

%Set up partition function
Q_T_Ref = Q(296,2,1,PAR_Data);
Q_T = Q(T,2,1,PAR_Data);
c2 = 1.4388;    % [cm K]

%Calculateall total line strength from all CO2 lines in the region of
%interest
S = 0;
for i=1:1:size(S_ref,1)
    S = S + S_ref(i)*Q_T_Ref/Q_T*(296/T)*exp(-c2*E(i)/T)/exp(-c2*E(i)/296)*...
        (1-exp(-c2*nu_line(i)/T))/(1-exp(-c2*nu_line(i)/296));
end

%Find concentration
X=(A/P)/(S*7.338933E21/T)/(2.54*2);
%Determine error
dSig=diff(Sig);
dnu=diff(nu);
```

```
44 firstderiv=dSig./dnu(end:-1:1);
45 Maxerr=max(diff(firstderiv)./dnu(end:-1:2));
46 Err =Maxerr.*((nu(end)-nu(1))/(12*size(nu,1).^2));
47
48 %Calculation of partition function
49 function [par] = Q(T,Mol,Iso,PAR_Data);
50
51
52
53 if Mol==1
54     if Iso==1
55         ind=2;
56     elseif Iso==2
57         ind=3;
58     elseif Iso==3
59         ind=4;
60     elseif Iso==4
61         ind=5;
62     elseif Iso==5
63         ind=6;
64     elseif Iso==6
65         ind=7;
66     end
67 elseif Mol==2
68     if Iso==1
69         ind=1+7;
70     elseif Iso==2
71         ind=2+7;
72     elseif Iso==3
73         ind=3+7;
74     elseif Iso==4
75         ind=4+7;
```

```
76      elseif Iso==5
77          ind=5+7;
78      elseif Iso==6
79          ind=6+7;
80      elseif Iso==7
81          ind=7+7;
82      elseif Iso==8
83          ind=8+7;
84      end
85  elseif Mol==5
86      if Iso==1
87          ind=39;
88      elseif Iso==2
89          ind=40;
90      elseif Iso==3
91          ind=41;
92      elseif Iso==4
93          ind=42;
94      elseif Iso==5
95          ind=43;
96      elseif Iso==6
97          ind=44;
98      end
99  elseif Mol==8
100     if Iso==1
101         ind=51;
102     elseif Iso==2
103         ind=52;
104     elseif Iso==3
105         ind=53;
106     end
107 elseif Mol==10
```

```
108     if Iso==1
109         ind=56;
110     end
111 end
112
113 par = interp1(PAR_Data.data(:,1),PAR_Data.data(:,ind),T);
```

6.3 Stoichiometric Calculations

6.3.1 Methane.

THE balanced chemical equation is,

$$CH_4 + 2\,O_2 \rightarrow CO_2 + 2\,H_2O \tag{6.1}$$

Using a molar mass for air of approximately 29 g/mol and a molar mass for methane of 16 g/mol, this yields a fuel to air (given air is approximately 21% O_2) ratio in stoichiometric conditions of $(\frac{m_{fuel}}{m_{oxidizer}})_{st} = 0.058$.

6.3.2 Ethane.

THE balanced chemical equation is,

$$2\,C_2H_6 + 7\,O_2 \rightarrow 4\,CO_2 + 6\,H_2O \tag{6.2}$$

Using a molar mass for air of approximately 29 g/mol and a molar mass for methane of 30 g/mol, this yields a fuel to air (given air is approximately 21% O_2) ratio in stoichiometric conditions of $(\frac{m_{fuel}}{m_{oxidizer}})_{st} = 0.062$.

6.3.3 Propane.

THE balanced chemical equation is,

$$C_3H_8 + 5\,O_2 \rightarrow 3\,CO_2 + 4\,H_2O \tag{6.3}$$

Using a molar mass for air of approximately 29 g/mol and a molar mass for methane of 44 g/mol, this yields a fuel to air (given air is approximately 21% O_2) ratio in stoichiometric conditions of $(\frac{m_{fuel}}{m_{oxidizer}})_{st} = 0.064$.

Bibliography

[1] URL http://www.thorlabs.com/newgrouppage9.cfm?objectgroup_id=4804.

[2] URL http://irassociates.com/index.php?page=hgcdte.

[3] Barron-Jimenez, R, JA Caton, TN Anderson, RP Lucht, Th Walther, S Roy, MS Brown, and JR Gord. "Application of a difference-frequency-mixing based diode-laser sensor for carbon monoxide detection in the 4.4–4.8 μm spectral region". *Applied Physics B*, 85(2-3):185–197, 2006.

[4] Bernath, Peter F. *Spectra of Atoms and Molecules*. Oxford University Press, second edition, 2005.

[5] Bradshaw, JL, NP Breznay, JD Bruno, JM Gomes, JT Pham, FJ Towner, DE Wortman, RL Tober, CJ Monroy, and KA Olver. "Recent progress in the development of type II interband cascade lasers". *Physica E: Low-dimensional Systems and Nanostructures*, 20(3):479–485, 2004.

[6] Brown, Michael S, Skip Williams, Chadwick D. Lindstrom, and Dominic L. Barone. *Progress in Applying Tunable Diode Laser Absorption Spectroscopy to Scramjet Isolators and Combustors*. Technical report, AFRL Propulsion Directorate, May 2010.

[7] Chang, Leyen S, Christopher L Strand, Jay B Jeffries, Ronald K Hanson, Glenn S Diskin, Richard L Gaffney, and Diego P Capriotti. "Supersonic Mass-Flux Measurements via Tunable Diode Laser Absorption and Nonuniform Flow Modeling". *AIAA Journal*, 49(12):2783–2791, 2011.

[8] Demtroder, Wolfgang. *Laser Spectroscopy Volume 2: Experimental Techniques*, volume 2. Springer, fourth edition, 2008.

[9] Engel, Thomas. *Quantum Chemistry and Spectroscopy*. Pearson Education, 2012.

[10] Faist, Jerome, Federico Capasso, Deborah L Sivco, Carlo Sirtori, Albert L Hutchinson, and Alfred Y Cho. "Quantum cascade laser". *Science*, 264(5158):553–556, 1994.

[11] Farooq, Aamir, Hejie Li, Jay B Jeffries, and Ronald K Hanson. "Measurements of CO2 and H2O near 2.7 μm using Tunable Diode Laser Absorption". *43rd AIAA/ASME/SAE/ASEE Joint Propulsion Conference & Exhibit. Cincinnati, USA: AIAA*, volume 5015, 1–5015. 2007.

[12] George, T., W. Urban, and A. Lefloch. "Improved Mass-Independent Dunham Parameters for the Ground State of {CO} and Calibration Frequencies for the

Fundamental Band". *Journal of Molecular Spectroscopy*, 165(2):500 – 505, 1994. ISSN 0022-2852. URL http://www.sciencedirect.com/science/article/pii/S0022285284711532.

[13] Goldenstein, Christopher S, Ian A Schultz, Jay B Jeffries, and Ronald K Hanson. "TDL Absorption Sensor for Temperature Measurements in High-Pressure and High-Temperature Gases". *50th AIAA Aerospace Sciences Meeting including the New Horizons Forum and Aerospace Exposition*, 2012.

[14] Heumier, T.A. and J.L. Carlsten. *Mode Hopping in Semiconductor Lasers*. Application note, ILX Lightwave: Photonic Test and Measurement Instrumentation, 2003.

[15] Jomaas, G, XL Zheng, DL Zhu, and CK Law. "Experimental determination of counterflow ignition temperatures and laminar flame speeds of C2–C3 hydrocarbons at atmospheric and elevated pressures". *Proceedings of the Combustion Institute*, 30(1):193–200, 2005.

[16] Kawahara, Nobuyuki, Eiji Tomita, Atsushi Ohtsuki, and Yuzo Aoyagi. "Cycle-resolved residual gas concentration measurement inside a heavy-duty diesel engine using infrared laser absorption". *Proceedings of the Combustion Institute*, 33(2):2903–2910, 2011.

[17] Kraetschmer, Thilo, Andrew W Caswell, Keith D Rein, Scott T Sanders, Sukesh Roy, Dale T Shouse, Barry V Kiel, and James R Gord. "Multi-spectral, multi-path absorption spectroscopy at 30 kHz using time-division multiplexed lasers". *47th AIAA Aerospace Sciences Meeting*. 2009.

[18] Meyer, Terrence R, Sukesh Roy, Thomas N Anderson, Joseph D Miller, Viswanath R Katta, Robert P Lucht, and James R Gord. "Measurements of OH mole fraction and temperature up to 20 kHz by using a diode-laser-based UV absorption sensor". *Applied Optics*, 44(31):6729–6740, 2005.

[19] Ombrello, Timothy, Campbell Carter, and Viswanath Katta. "Burner platform for sub-atmospheric pressure flame studies". *Combustion and Flame*, 159(7):2363–2373, 2012.

[20] Ren, W, A Farooq, DF Davidson, and RK Hanson. "CO concentration and temperature sensor for combustion gases using quantum-cascade laser absorption near 4.7 μm". *Applied Physics B*, 107(3):849–860, 2012.

[21] Rhoby, M, Kevin C Gross, and David L Blunck. "Application of an Imaging Fourier-Transform Spectrometer to Determine Two-Dimensional Scalar Values in Laminar Flames". *Spring Technical Meeting of the Central States Section of the Combustion Institute*. 2012.

[22] Rieker, GB, H Li, X Liu, JTC Liu, JB Jeffries, RK Hanson, MG Allen, SD Wehe, PA Mulhall, and HS Kindle. "Rapid measurements of temperature and H2O concentration in IC engines with a spark plug-mounted diode laser sensor". *Proceedings of the Combustion Institute*, 31(2):3041–3049, 2007.

[23] Rieker, Gregory B, Jay B Jeffries, and Ronald K Hanson. "Calibration-free wavelength-modulation spectroscopy for measurements of gas temperature and concentration in harsh environments". *Applied Optics*, 48(29):5546–5560, 2009.

[24] Rothman, Larry S, CP Rinsland, A Goldman, ST Massie, DP Edwards, JM Flaud, A Perrin, C Camy-Peyret, V Dana, J-Y Mandin, et al. "The HITRAN molecular spectroscopic database and HAWKS (HITRAN Atmospheric Workstation): 1996 edition". *Journal of Quantitative Spectroscopy and Radiative Transfer*, 60(5):665–710, 1998.

[25] Rothman, LS, IE Gordon, RJ Barber, H Dothe, RR Gamache, A Goldman, VI Perevalov, SA Tashkun, and J Tennyson. "HITEMP, the high-temperature molecular spectroscopic database". *Journal of Quantitative Spectroscopy and Radiative Transfer*, 111(15):2139–2150, 2010.

[26] Schultz, Ian A, Christopher S Goldenstein, Jay B Jeffries, Ronald K Hanson, Robert D Rockwell, and Christopher P Goyne. "TDL Absorption Sensor for In Situ Determination of Combustion Progress in Scramjet Ground Testing". *28th Aerodynamic Measurement Technology, Ground Testing, and Flight Testing Conference*. 2012.

[27] Torek, Paul V, David L Hall, Tiffany A Miller, and Margaret S Wooldridge. "H2O Absorption Spectroscopy for Determination of Temperature and H2O Mole Fraction in High-Temperature Particle Synthesis Systems". *Applied Optics*, 41(12):2274–2284, 2002.

[28] Varshni, YP. "Temperature dependence of the energy gap in semiconductors". *Physica*, 34(1):149–154, 1967.

[29] Zeller, Wolfgang, Lars Naehle, Peter Fuchs, Florian Gerschuetz, Lars Hildebrandt, and Johannes Koeth. "DFB Lasers Between 760 nm and 16 μm for Sensing Applications". *Sensors*, 10(4):2492–2510, 2010.

[30] Zhou, Xin, Jay B Jeffries, Ronald K Hanson, Guoqiang Li, and Ephraim Gutmark. "Wavelength-scanned tunable diode laser temperature measurements in a model gas turbine combustor". *AIAA Journal*, 45(2):420–425, 2007.

Vita

Stephen Daniel Wakefield grew up in Gilcrest, Colorado where he graduated from high school. Upon graduation of high school he attended the United States Air Force Academy. After four years he received recognition as a distinguished graduate with a bachelor's degree in Physics as well as Mathematics and with a minor in Russian. He was commissioned as a Second Lieutenant in the United States Air Force. Upon graduation and commissioning he was assigned to the Air Force Institute of Technology to pursue a Master's degree in Applied Physics. Upon completion of his Master's program, he will be attending Euro-NATO Joint Jet Pilot Training at Sheppard AFB, TX.

REPORT DOCUMENTATION PAGE

Form Approved
OMB No. 0704-0188

PLEASE DO NOT RETURN YOUR FORM TO THE ABOVE ORGANIZATION.

1. REPORT DATE *(DD-MM-YYYY)*	2. REPORT TYPE	3. DATES COVERED *(From - To)*
27-03-2014	Master's Thesis	Oct 2012 - Mar 2014

4. TITLE AND SUBTITLE
Development and Characterization of a High Speed Mid-IR Tunable Diode Laser Absorption Spectrometer for CO and CO2 Detection in Detonation Events

5a. CONTRACT NUMBER

5b. GRANT NUMBER

5c. PROGRAM ELEMENT NUMBER

6. AUTHOR(S)
Wakefield, Stephen D., Second Lieutenant, USAF

5d. PROJECT NUMBER

5e. TASK NUMBER

5f. WORK UNIT NUMBER

7. PERFORMING ORGANIZATION NAME(S) AND ADDRESS(ES)
Air Force Institute of Technology
Graduate School of Engineering and Management (AFIT/EN)
2950 Hobson Way
Wright-Patterson AFB OH 45433-7765

8. PERFORMING ORGANIZATION REPORT NUMBER
AFIT-ENP-14-M-38

9. SPONSORING/MONITORING AGENCY NAME(S) AND ADDRESS(ES)
"Intentionally Left Blank"

10. SPONSOR/MONITOR'S ACRONYM(S)

11. SPONSOR/MONITOR'S REPORT NUMBER(S)

12. DISTRIBUTION/AVAILABILITY STATEMENT
Distribution Statement A. APPROVED FOR PUBLIC RELEASE; DISTRIBUTION UNLIMITED.
Other requests for this document shall be referred to AFIT ENP Office 2950 Hobson Way Wright-Patterson AFB, OH 45433-7765.

13. SUPPLEMENTARY NOTES
This material is declared work of the U.S. Government and is not subject to copyright protection in the United States.

14. ABSTRACT
A tunable diode laser absorption spectroscopy system, capable of collecting data at a 10 kHz repetition rate near 4.5 μm. This system was made feasible in recent years due to the development of quantum cascade lasers active in the 4.5 μm region of the spectrum. Reaching into the mid-IR region of the electromagnetic spectrum allowed for an analysis of the fundamental absorption bands for both CO and CO2. The spectral absorption was measured for ethylene, methane, ethane, and propane across a variety of equivalence ratios, at various heights above a Hencken Burner surface. For each fuel, the concentration of CO2 was found to agree with chemical equilibrium analysis (CEA) calculations within approximately 8%. The concentration for CO agreed with CEA but with larger error bounds at approximately 20%. It is believed that such large error can be attributed to taking measurements on a hot band, as well as large amounts of H2O and CO2 absorption in the area. This ultimately resulted the measurement of combustion efficiency, which agreed with expected results with approximately 10% error bounds. With this system's proof of concept, it will be possible to analyze real combustors as well as detonation events.

15. SUBJECT TERMS
TDLAS, Mid IR, 10 kHz, CO, CO2

16. SECURITY CLASSIFICATION OF:			17. LIMITATION OF ABSTRACT	18. NUMBER OF PAGES	19a. NAME OF RESPONSIBLE PERSON
a. REPORT	b. ABSTRACT	c. THIS PAGE			Col. Brian A. Tom, AFIT/EN
U	U	U	UU	109	19b. TELEPHONE NUMBER *(Include area code)* (937) 785-3636 x7112 brian.tom@afit.edu